Master's Thesis
30 credits

Non-linear effects in the ATLAS track-counting luminosity measurement

Daniel Nikolas Gautam

Uppsala, November 6, 2023

UPPSALA UNIVERSITET

Uppsala University
Supervisor: Giulia Ripellino
Subject Reader: Rebeca Gonzalez Suarez

Abstract

In this thesis the linearity of the ATLAS track-counting luminosity measurement is studied using two different sets Monte Carlo simulated crossings of proton-proton bunches. A primary high-momentum, or hard, interaction must be chosen for the Monte Carlo simulation. The first of the two sets is simulated using $Z \to \mu\mu$ as primary hard scatter in the bunch crossings while the second set is simulated with a single neutrino particle gun as the primary hard scatter. The luminosity can be determined by track counting from the relationship between the number of reconstructed charged particle tracks and the number of proton-proton interactions per bunch crossing in the ATLAS detector. The relationship between the two is theoretically linear but is affected by non-linear effects from the presence of fake tracks and the reduced tracking efficiency at large μ.

The linearity is studied and compared for eight different sets of track selection criteria called working points. Four of the working points were used during Run 2 of the Large Hadron Collider and four are introduced for Run 3.

It is found that the use of the physical hard scatter, $Z \to \mu\mu$, in the Monte Carlo generation results in the appearance of tracks at all interaction rates, to a degree that does not agree with experiment. The use of the single neutrino particle gun for the simulation of hard scatter interactions is found to be more suitable for the track counting studies.

Two of the working points introduced for Run 3, called *TightModHighPtStrictLumi* and *TightModFullEtaHighPtStrictLumi*, are found to outperform the rest of the working points.

Keywords: Particle physics, CERN, ATLAS, Track counting, Luminosity, Monte Carlo, Track Selection

Sammanfattning

I denna uppsats studeras linjäriteten av en luminositet-mätningsmetod kallad track-counting som används vid ATLAS-detektorn. Linjäriteten studeras för två olika uppsättningar av simulerade proton-protonkollisioner. Kollisionerna produceras med hjälp av Monte Carlo-simuleringar. Den första uppsättningen simuleras användandes $Z \rightarrow \mu\mu$ som mest högenergetisk interaktion i alla event medan den andra uppsättningen istället simuleras användandes en högenergetisk neutrinopartikel i alla event. Med hjälp av track-counting bestäms luminositeten genom förhållandet mellan antalet rekonstruerade laddade partikelspår och antalet proton-protoninteraktioner per ”bunch crossing” i ATLAS-detektorn. I teorin är relationen mellan de två linjär, men track-counting metoden påverkas av icke-linjära effekter såsom falskt rekonstruerade partikelspår och minskad effektivitet vid stora μ-värden. Linjäriteten studeras och jämförs för åtta olika uppsättningar av kriterier som appliceras på partikelspåren.

Linjäriteten jämförs for åtta olika uppsättningar av spårkriterier som kallas ”Working points”. Fyra Working points har tidigare använts under den andra körningen av ”the Large Hadron Collider” medan fyra Working points är introducerade inför den tredje körningen.

Användningen av uppsättningen kollisioner som simuleras med $Z \rightarrow \mu\mu$ som mest högenergetisk interaktion resulterar i spår vid alla μ-värden till en grad som inte överensstämmer med förväntningar. Användningen av neutrinopartikeln som mest högenergetsik interaktion vid simulering av event visar sig vara mer lämplig för studier som berör track-counting.

Två av de Working points som introducerades inför den tredje körningen av ”The Large Hadron Collider” visar sig prestera bättre än de andra. Dessa Working points har namnen *TightModHighPtStrictLumi* och *TightModFullEtaHighPtStrictLumi*.

Acknowledgements

I want to give many thanks to my supervisor Giulia for your continued support and patience throughout this project, I could not have asked for a better supervisor.

To my family and friends who always cheer me on, thank you all, I could not have done this without you.

Contents

1 Introduction

The Large Hadron Collider (LHC) at CERN is the world's largest particle accelerator and collider and ATLAS is one of the main experiments that studies its particle collisions. The luminosity is a measure used to describe the number of particles produced in collisions in particle experiments such as ATLAS. Precise luminosity measurements are vital for every ATLAS analysis, and one of the most important methods for measuring the luminosity is track-counting (TC). The basic principle of TC is the counting of the number of charged particles that pass through, in this case, the innermost part of the ATLAS detector. There is in theory a linear relationship relationship between the number of tracks and the actual number of colliding protons per bunch crossing. Due to effects such as the fake track rate and tracking efficiency this linear relationship does not hold in reality.

The understanding of these effects on the TC measurement is important for reducing uncertainties and for improving track selection. In this thesis, these effects are examined with the use of two different sets of Monte Carlo (MC) simulated proton-proton collisions.

TC is used to determine the long term stability (luminosity calibration over time) and serves as a reference for the calibration transfer (transfer of measurements from the low- to high-luminosity regime) of other luminosity sensitive systems at ATLAS [1]. The TC luminosity measurement is based on the detection of charged particles, reconstructed as tracks, which makes it dependent on the chosen track selection criteria.

Eight different sets of track selection criteria, called Working Points (WPs), are studied in this thesis. Four of them were used during the second operational period of the LHC, Run 2, and four were created for Run 3, which is ongoing as of the writing of this thesis.

1.1 Authors contribution

The author has been given two different sets of simulated events which have been used to conduct TC studies. The two sets are compared and evaluated in terms of usefulness in TC studies. The linearity of the different WPs is studied. The WPs are compared and the two most promising WPs are picked out. All plots are generated by the author unless indicated otherwise. For the duration of this work the author is integrated in the luminosity group of ATLAS.

2 The Standard Model

There are different ways to describe how the universe works depending on the scale at which one is looking. In everyday life our world is well described by Newtonian physics, but exploring more extreme environments and astronomical scales often requires insight from Einsteins theory of relativity. Going to the most fundamental, smallest scales we have yet another view based on the Standard Model of particle physics, which describes the particles that make up our world and their interactions with eachother.

2.1 Overview of SM particles

The SM [2] is the most successful description of the universe at small scales. It is a theoretical framework that describes how particles interact with eachother. The particle content of the SM is summarised in Figure 2.1. It can be divided into two categories, bosons and fermions [3].

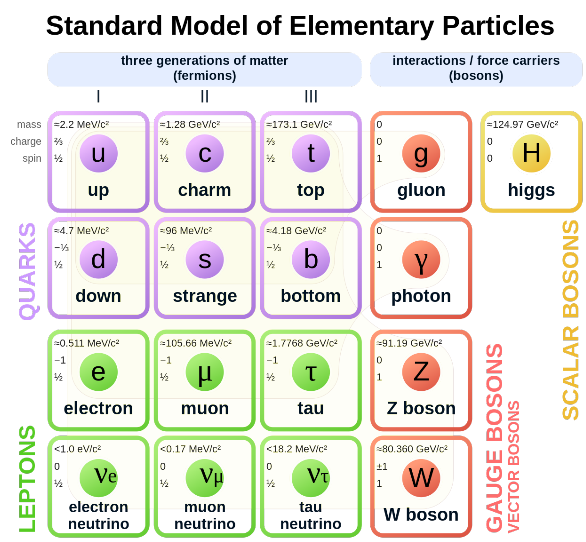

Figure 2.1: The Standard Model of elementary particles [4].

Bosons are particles with integer spin quantum number that follow Bose-Einstein statistics. They are the force carriers, mediating interactions between particles. There are five different elementary bosons in the SM, one scalar boson and four vector bosons.

The Higgs boson, H, is the only scalar boson. It has a spin of zero and is a result of the Higgs mechanism that is responsible for making otherwise massless particles massive [5].

The are four vector bosons. The photon, γ, is responsible for the electromagnetic interaction, the gluons, g, govern the strong interaction and the W and Z bosons are responsible for the weak interaction. Vector bosons all have a spin of one.

The Fermions all have half-integer spin and follow Fermi-Dirac statistics. They are the particles that make up all of the matter in the universe. Fermions are divided into three generations of increasing mass which are further divided into two groups, quarks and leptons.

The Quarks are spin-$\frac{1}{2}$ particles that together with gluons build hadrons, such as the proton and neutron, that make up most of the matter we interact with every day. The first generation contains the lightest quarks, the up and down, the second generation consists of the charm and strange, and the third generation of the top and bottom. The quarks have different electric charges. The up, charm and top quarks all have an electric charge of $+\frac{2}{3}\ e$, where e is the charge of the electron. The down, strange and bottom have a charge $-\frac{1}{3}e$. Quarks cannot be observed independently but are confined to hadrons.

The three Lepton generations each consist of one charged and one neutral particle. The charged particles are the electron, muon and tau and the neutral particles are the electron neutrino, muon neutrino and tau neutrino which in the SM are described as massless.

Although the SM is extremely successful it is not a complete theory. Some shortfalls of the SM are that the force of gravity is not incorporated and neither does it offer a suitable candidate for Dark matter or dark energy, all of which we observe to exist. It also fails to offer an explanation for neutrino mass.

2.2 Phenomenology of *pp* interactions

This thesis uses proton-proton (pp) collisions. Protons are stable composite particles, made of three valance quarks, namely two up quarks and one down quark, that are held together by the strong nuclear force. The gluons that mediate this force can spontaneously split to create colorless quark-antiquark pairs, surrounding the valance quarks by so called sea quarks.

Colliding protons at high energies can result in inelastic collisions causing the protons breaking up into their constituent parts, called partons. If the collision energy is high enough this can even lead to the creation of new particles according to Einsteins equation $E = mc^2$. These types of collisions are called hard interactions. The resulting particle landscape after these inelastic pp collisions can be described theoretically by the phenomenology of the interaction.

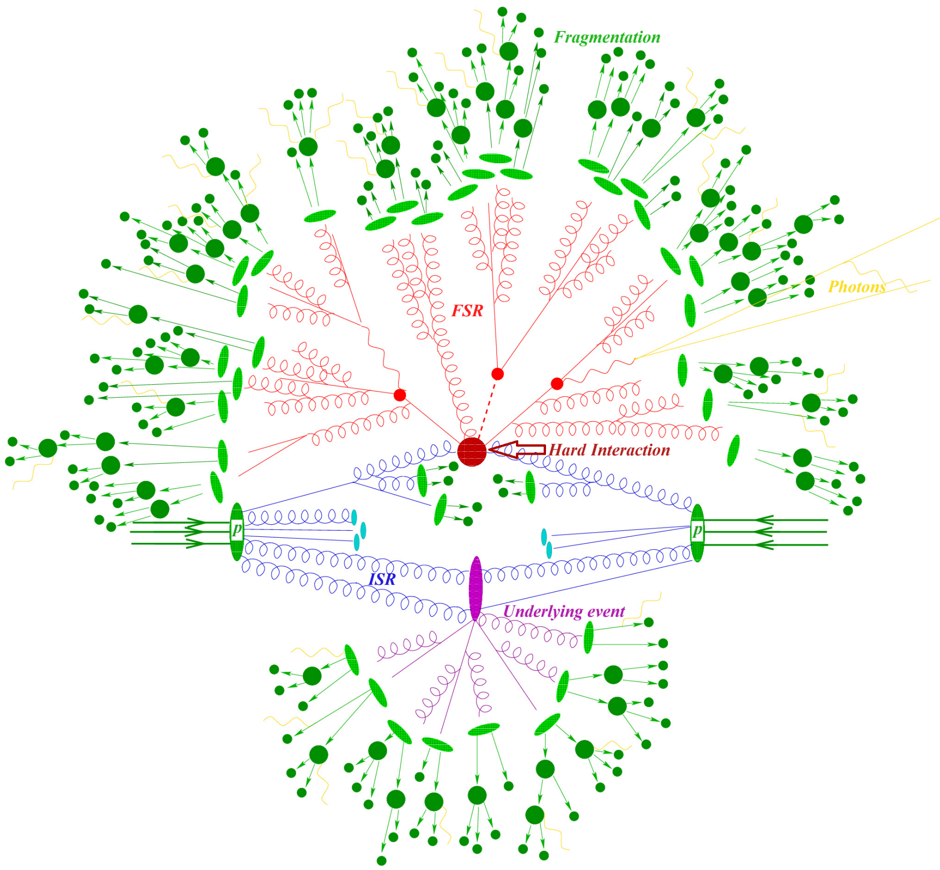

Figure 2.2: Illustration of the phenomenology of a pp collision. [6].

When protons collide at energy scales much larger than the hadronization scale ($Q^2 >> 200$ MeV) the constituents of the protons, called partons, act as free elementary particles. The fundamental interaction takes place between these partons and the energy of the collision is described by parton distribution functions (PDFs) [7]. The PDFs are probability distributions extracted from experiment [8], that are used to calculate production cross sections of hadron collisions. Figure 2.2 shows an illustration depicting a pp collision. The colliding protons are seen coming from the left and right sides of the figure, depicted by three green arrows pointing to green ovals marked with "p". The Initial State Radiation (ISR) is shown in blue and consists of particles radiated from the quarks and glouns making up the protons. The hard interaction is seen as the large red circle in the center of the figure, and leads to Final State Radiation (FSR) being emitted, also shown in red. Photons are also emitted by electrically charged particles as part of the FSR, shown in yellow. The next step is called fragmentation, where the particles combine to form hadrons, green ellipses, which decay if they are unstable. The underlying event, shown in purple, describes the interactions of the initial partons that were not part of the hard scatter.

3 Experimental setup

This section will give the reader an understanding of some of the important concepts necessary for understanding of later chapters such as the Large Hadron Collider, the ATLAS detector and luminosity.

3.1 The Large Hadron Collider

The Large Hadron Collider (LHC) [9] was constructed by CERN between 1998 and 2008 and is located close to the city of Geneva at the border of Switzerland of France. The LHC is a circular particle collider with a circumference of 27 km and built as deep as 175 m underground [10]. It is the largest machine in the world and is the most powerful particle accelerator so far. The LHC accelerates two particle beams in opposite directions to speeds close to the speed of light. The beams are steered around the LHC with the help of superconducting dipole magnets. The superconducting property of the magnets allow them to generate much stronger magnetic fields than regular magnets, increasing the amount that each magnet can bend the beam and effectively reducing the total length of the LHC. Quadrupole magnets are used to focus the beams along their path around the ring, for as the beams would otherwise spread out until they hit the walls of the beam pipe and disappeared. In total more than 50 different types of magnets are used to precisely control the beams to avoid losses in both speed and particle count [9].

Before the beams enter the LHC they are pre-accelerated in a series of smaller linear and circular accelerators that successively increase the speed and energy of the particles. After being accelerated to the maximum speed of one accelerator the particles are injected into the next until they reach the LHC. This system is called an injector chain.

The LHC is capable of circulating beams made of protons or of heavy ions such as lead nuclei. The beams are not a continuous stream of particles but consists instead of separated bunches of particles. During operation with proton beams there are around $1.6 \cdot 10^{11}$ protons per bunch [11] and around 2400 bunches circulating in the ring.

The beams cross each other only at specific locations around the ring, called interaction points (IP), where large detectors are built to collect valuable scientific data of the resulting particle collisions. The LHC has four main detectors, two multipurpose detectors, called ATLAS [12] and CMS [13]. ALICE is a detector mainly used in collisions of heavy ions. Lastly there is the LHCb detector.

So called insertion magnets focus the beams further and direct them towards eachother before every IP. The beams cross eachother at an angle, called the crossing angle, which can be adjusted if needed. This is necessary in order to prevent the beams from interacting too much before they reach the IP [14]. The crossing angle is small, around 150 microradians.

The LHC successfully steered a beam of protons around the ring for the first time on

September 10th, 2008. The LHC is helping us get answers to fundamental questions about the nature of the universe and has in its more than a decade long operation seen a number of never before seen particle interactions and also discovered the Higgs boson in 2012, previously predicted in 1964 [15].

3.2 Luminosity

One of the most important parameters for any particle collider is the luminosity. It provides a measure of the amount of data that an accelerator produces [16].

The instantaneous luminosity, $\mathcal{L}$, is proportional to the rate of events, $\frac{dR}{dt}$, as

$$\mathcal{L} \cdot \sigma_e = \frac{dR}{dt}, \tag{3.1}$$

with the cross section for events of interest, σ_e as proportionality factor, giving luminosity the unit of $\text{cm}^{-2}\text{s}^{-1}$.

It can be given by:

$$\mathcal{L} = \frac{N_b^2 n_b f_r F}{4\pi\sigma^2}, \tag{3.2}$$

where N_b is the number of protons per bunch, n_b is the number of bunch pairs, f_r is the revolution frequency and σ is the transverse beam width. F is a geometric factor that takes into account the change in transverse bunch size due to the non-zero beam crossing angle, which causes a change in luminosity.

The LHC is not only the worlds largest and highest energy particle accelerator, it also achieves the highest instantaneous luminosity of any hadron collider. The instantaneous luminosity is often simply referred to as the *luminosity*, as will be done in this thesis from this point on.

Another important measure is the integrated luminosity, which refers to the accumulated luminosity over some specified time interval. Naturally it is thus given by the time integral of the luminosity:

$$L_{int} = \int \mathcal{L}\ dt. \tag{3.3}$$

The integrated luminosity is often given in units of inverse femtobarn, fb^{-1}, instead of cm^{-2} and the two are related as $1\ \text{fb}^{-1} = 10^{39}\ \text{cm}^{-2}$.

The interesting processes in the case of this thesis are inelastic pp collisions. Denoting the cross section for inelastic pp interactions as σ_{inel}, we have the following relationship for the luminosity in pp collisions per bunch crossing:

$$\mathcal{L} = \frac{\mu \cdot f_r}{\sigma_{inel}}, \tag{3.4}$$

where f_r is the revolution frequency of protons in the LHC ring and μ is the *pileup parameter* denoting the average number of inelastic particle interactions and is linearly proportional to the luminosity.

Luminosity is determined by beam parameters such as the number of protons per bunch, number of bunches, revolution frequency, beam size and crossing angle. LUCID and BCM are the main ones used, discussed in Section 4.1. The ATLAS detector, discussed in section 3.3, has many luminosity sensitive systems.

At high luminosity levels several pp interactions take place in each bunch crossing. The most energetic interaction is called the hard interaction and the additional ones are called pileup interactions. There is in-time and out-of-time pileup. In-time pileup refers to pp collisions that occur in the same BC as the hard primary collision of interest. Out-of-time pileup refers instead to pp collisions that occur in the BCs immediately before or after the collision of interest.

The pileup parameter, μ, is a measure of the number of pileup interactions in each bunch crossing. Under typical Run 2 conditions $\mu \simeq 30$ for pp collisions, see Figure 3.6.

The pileup parameter corresponds to the mean of a Poisson probability distribution of the true number of particle interactions per bunch crossing, N_{int}, given by

$$P(N_{int}) = \frac{e^{-\mu} \cdot \mu^{N_{int}}}{N_{int}!}. \tag{3.5}$$

3.2.1 Operational periods

In March 2010, ATLAS recorded pp collisions with a center of mass (CoM) energy of 7 TeV [17] for the first time [12], a CoM energy more than three times higher than the previous record for any particle accelerator. Just over a year later, in 2012, the LHC provided collision energies of 8 TeV before concluding Run 1 in early 2013, marking the beginning of Long Shutdown 1 (LS1). The total integrated luminosity delivered to ATLAS during Run 1 was 5 fb^{-1} at 7 TeV and 20 fb^{-1} at 8 TeV.

During LS1, changes were made to the LHC to enable collisions with a CoM energy of 13 TeV before Run 2, which began in 2015 and continued until 2018.

Long Shutdown 2 (LS2) lasted until 2022 when Run 3 started up operations again with 13 TeV CoM collisions [18]. Run 3 is not yet concluded as of the writing of this thesis, but a third shutdown period is expected in the coming years during which further upgrades to the LHC are expected with the goal of significantly increasing luminosity. The total integrated luminosity delivered to ATLAS during Run 2 was 156 fb^{-1}, with a maximum instantaneous luminosity of 2×10^{34} cm^{-2}s^{-1}.

Run 3 is currently underway, operating at a CoM energy of 13.6 TeV, which is the highest of any particle accelerator in the world. Run 3 is planned to end in the year 2026 [19] followed by LS3 (2023-2029).

The LHC delivered a total integrated luminosity, $L_{int} = 38.5$ fb^{-1} during Run 3 in 2022 [20] and the total integrated luminosity delivered to ATLAS during Run 3, as of the writing of this thesis, is 70 fb^{-1}, see Figure 3.1 for a more detailed view of the ATLAS delivered luminosity for all runs with stable beams.

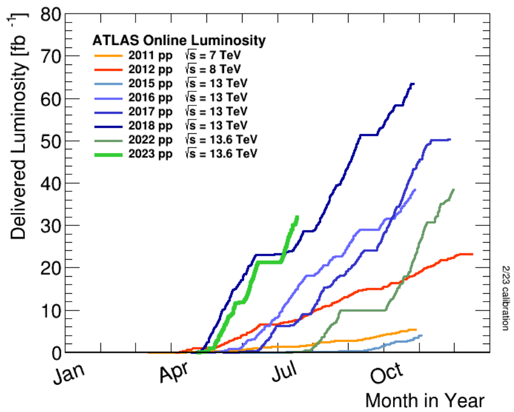

Figure 3.1: Cumulative luminosity per day delivered to ATLAS with stable beams and high energy *pp* collisions. [20]

During LS3, a high luminosity upgrade is planned for the LHC called the HL-LHC (High Luminosity LHC) [21]. Following these upgrades the LHC is expected to see an increase of at least a factor of 5 in the instantaneous luminosity yield compared to the current nominal value [22].

3.3 The ATLAS detector

The ATLAS detector [23] is the biggest detector ever built for a particle collider. The detector weighs around 7000 tonnes and has is cylindrical in shape, measuring 46m long and 25m in diameter. While in operation there are a billion particle collisions taking place per second within the detector, but only one per million of these are recorded as interesting.

3.3.1 Detector design

The ATLAS detector is made up of multiple subdetectors that are designed to detect different properties of the decay products produced in collisions, see Figure 3.2. The Tracking part of the detector is called the Inner Detector (ID) and is designed to detect charged particles that may pass through it and reconstruct their trajectories through the detector. By tracing these paths backwards, this information can be used to find the origins of collisions or decay points, called vertices.

Surrounding the ID is a superconducting solenoid magnet, followed by detector layer called the ATLAS calorimeter system, consisting of the Electromagnetic and the hadronic calorimeters, that is tasked with measuring the energy of particles. Among the particles that get detected by the calorimeter are photons, electrons, muons and hadrons, detected as jets.

Surrounding the center of the experiment is also a 25 meter long barrel toroid, which is the largest toroidal magnet ever built. It is accompanied by two end-cap toroids on either side of the experiment which can be seen in Figure 3.2.

The Muon spectrometer is the final detector layer of ATLAS and as the name suggests it is tasked with detecting muons and measuring their momentum. The spectrometer measures the direction and the momentum of passing muons [24].

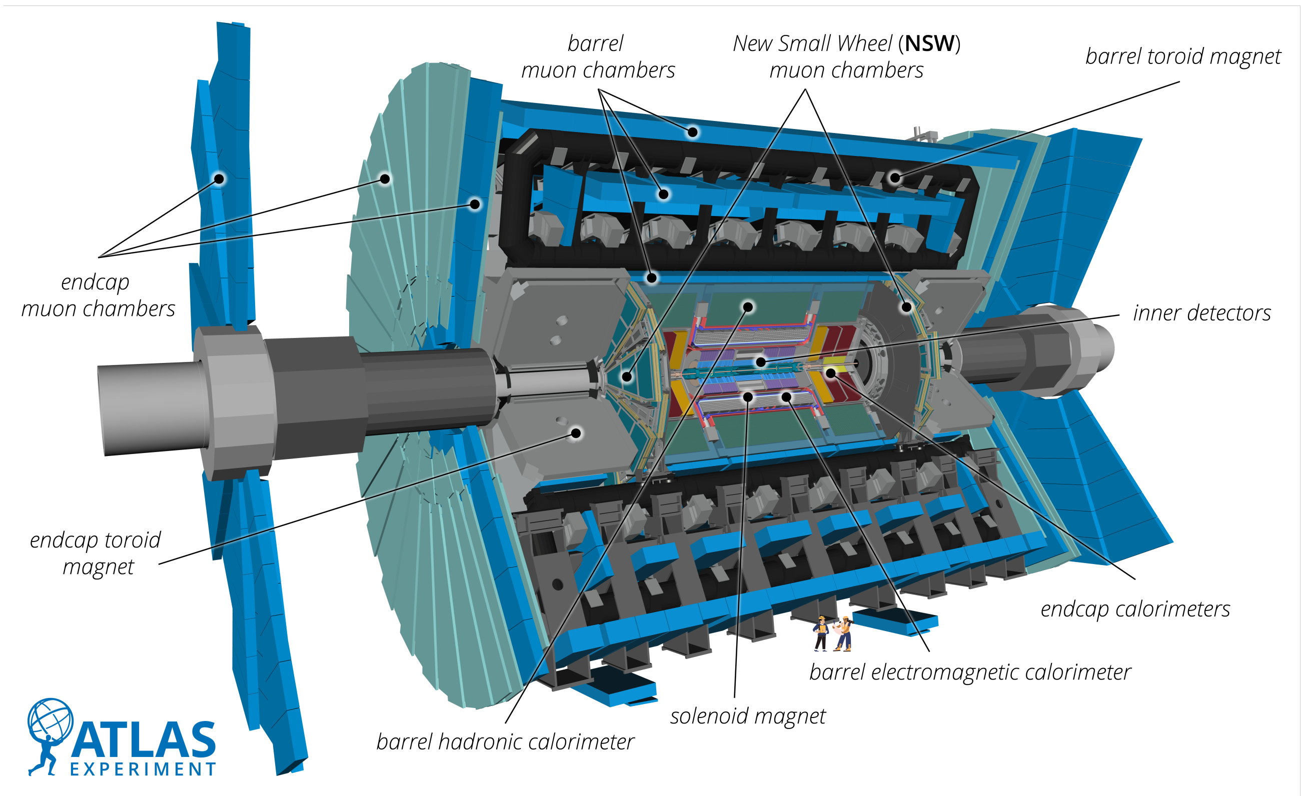

Figure 3.2: Schematic illustration of the ATLAS detector with labels describing highlighted parts [25].

The part of the ATLAS detector that is relevant for track-counting studies such as the work in this thesis is the ID.

3.3.2 ATLAS coordinate system

ATLAS uses right handed Cartesian coordinates with the x-axis pointing towards the center of the LHC ring. The z-axis runs along the beam pipe and the y-axis points upwards with a slight offset from vertical because of the slight tilt of the ATLAS tunnel [26].

The azimuthal angle ϕ is measured around the beam starting from the positive x-axis and the polar angle θ is measured from the positive z-axis. The ATLAS detector is designed to be symmetrical in θ.

The pseudorapidity, η, measures the angle of a particle relative to the beam axis and is defined as $\eta = -\ln(\tan(\theta/2))$.

The component of particle momenta that is perpendicular to the beam axis is the transverse momentum, denoted p_T. Since the colliding protons have no translational component in the transverse plane, all motion in this plane is the result of physics processes at the collision point.

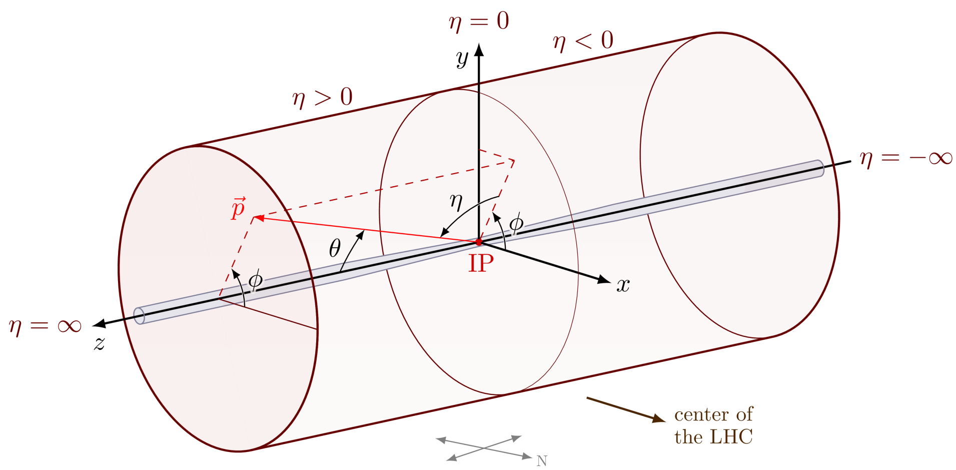

Figure 3.3: The coordinate system used for the ATLAS experiment [27].

3.3.3 Inner Detector

The Inner Detector (ID) is the part of the ATLAS detector system that is closest to the beam-beam IP and consists of three subdetectors [28].

The innermost subdetector is the Pixel detector made up of four layers of silicon pixels, at the average radii of ∼4 cm, 11 cm and 14 cm away from the IP, and three endcap layers on either side of the IP. The Pixel detector has very high granularity and is able to measure the origin of charged particles with a precision of 10 μm [29]. Having high granularity is most important close to the IP due to the high particle flux there.

The next layer of the ID is the Semiconductor Tracker, abbreviated SCT, consisting of four layers of silicon barrels (and nine silicon endcap discs) placed around the IP. The total area of the silicon barrel detectors is 61 m^2 with a spatial resolution in the Rϕ direction of 16 μm and 580 μm in the z direction.

The final layer of the ID is the Transition Radiation Tracker, the TRT. The TRT is a straw tube tracking detector with a barrel region and endcap discs [30]. They both consist of drift tubes, or straws, that are 4 mm in diameter and filled with a mixture of Xenon gas mixed with CO_2 and O_2 gas. A negative voltage is applied to the walls of the tubes and running along the center of these tubes is a gold-plated tungsten wire connected to ground. The barrel layers of the TRT is made up of straws 1.5 m in length while the endcap straws are 0.4 meters long and positioned perpendicular to the beam axis. Charged particles passing through the TRT ionize the gas inside the straws causing the freed electrons to drift to the wire from which a signal is registered in both ends. The space between the straws is filled with a radiator that may induce transition radiation whenever relativistic particles enter the medium.

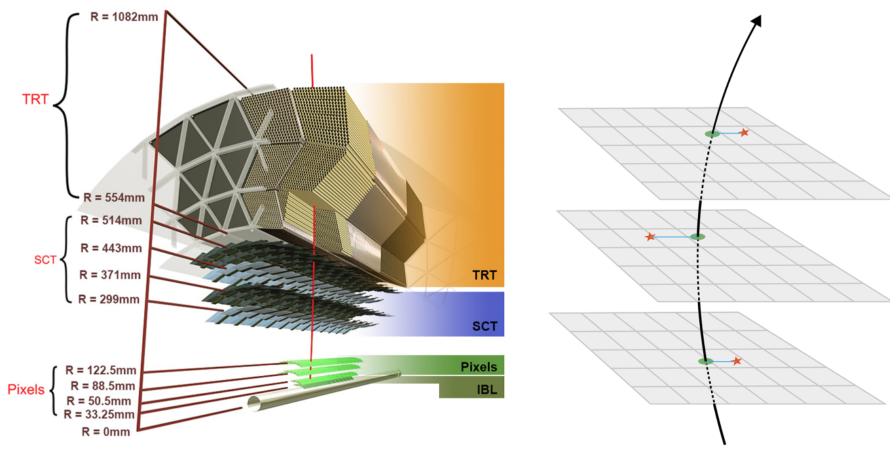

Figure 3.4: To the left is an illustration of the ATLAS Inner Tracking Detector system. The Pixel, SCT and TRT subdetectors are highlighted. To right figure is a schematic representation of a charged particle passing through sub-detector layers. The red stars indicate every detector measurement (hit). The reconstructed track is shown in black. The green dots indicate the intersection of the track with each surface. The blue lines show the offset of the fitted track and the hits [31].

3.3.4 ATLAS luminosity sensitive systems

There are multiple luminosity sensitive systems in ATLAS called *luminometers*. The Luminosity Cherenkov Integrating Detector (LUCID) and the Beam Conditions Monitor (BCM) are the two main luminometers. LUCID consists of two detector arms, one on each side of the beam-beam IP. On each arm, 4 groups of 4 photomultiplier tubes, that use quartz windows as Cherenkov medium, are positioned around the beam pipe [32]. The BCM measures luminosity using diamond sensors positioned about 2 metres from the IP [33]. The most capable luminometer of the ATLAS experiment is LUCID, able to reliably provide fast luminosity measurements for all beam configurations and over different luminosity ranges [32].

Besides using LUCID and BCM the luminosity can also be measured using information from the calorimeters and the ID, via track-counting . This offers redundancy in the luminosity measurement, important for validation cross checks and for reducing systematic uncertainties.

3.4 Event reconstruction

The various subsystems in ATLAS provide electronic signals that then need to be combined in order to reconstruct so-called physics objects representing the particles that passed through the detector. Figure 3.5 shows an illustration of how the different systems interact with some common particle types. The physics object relevant to this work is the track and the track reconstruction is described in Section 3.4.1.

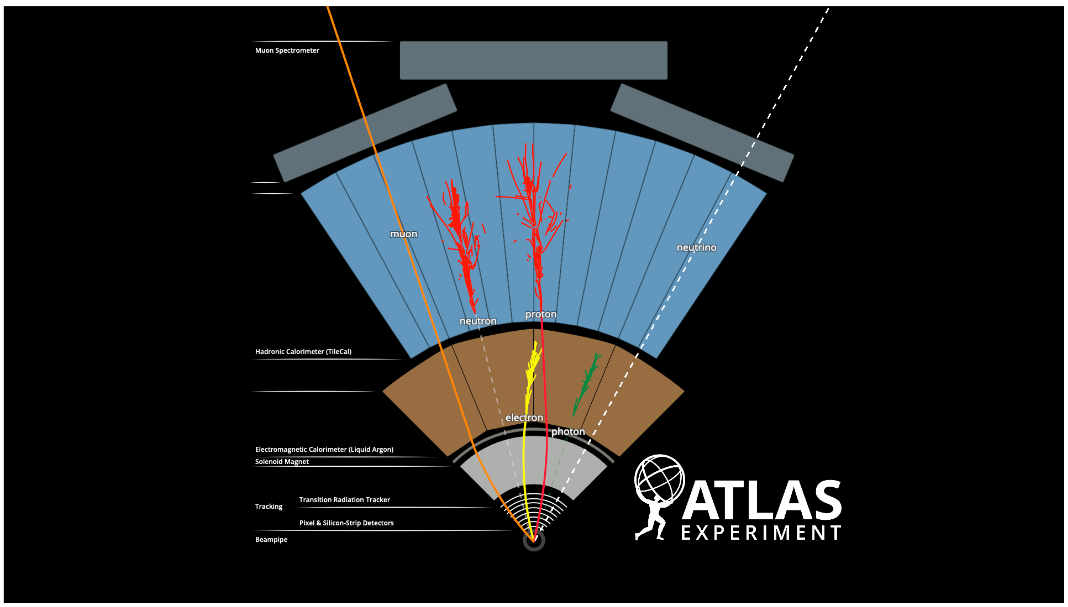

Figure 3.5: Illustration of the ATLAS detector. The interactions of different particles within the different subdetectors are also shown [34].

3.4.1 Track Reconstruction

When charged particles move through the magnetic fields in the Inner Detector they move in a predictable way depending on their momentum and charge. The track reconstruction takes advantage of this when trying to solve for particle paths from the recorded hits. The track reconstruction algorithms looks at hits in the Pixel and SCT detectors and combine hits using pattern recognition, before making use of a combinatorial Kalman filter to find potential track candidates. After this the track candidates are put through an ambiguity solver to refine the track selection further. Outside-in track reconstruction is then also performed in regions of interest [35].

To reconstruct the particle paths, five track parameters are needed, the transverse and longitudinal impact parameters d_0, z_0, the azimuthal and polar angles ϕ, θ of the track momentum and the ratio of the charge and the magnitude of the track momentum q/p.

The transverse impact parameter, d_0, is defined as the distance of closest approach between a reconstructed particle track and corresponding primary interaction vertex. The uncertainty in d_0 is denoted σ_{d_0} and the d_0-significance is defined as d_0/σ_{d_0}.

The value of the point on the z-axis that determines the position of d_0 is defined as the longitudinal impact parameter, z_0. The uncertainty in z_0 is denoted σ_{z_0} and the z_0-significance is defined as z_0/σ_{z_0}.

For definitions of the azimuthal and polar angles, ϕ and θ, see Section 3.3.2.

Each measured signal in the different strips and pixels of ID is assigned a 3D spacial coordinate, or space point, corresponding to the position of the part that was hit. These detector measurements are called hits and the information from these hits it is possible to retrace the particle trajectories, called tracks, by using track reconstruction algorithms.

The hits are combined (by a combinatorial Kalman filter [36]) with other hits possibly belonging to the same track, often resulting in several different track candidates per seed. By estimating the particle trajectories, each track is given a score based on its goodness of fit, favouring tracks with fewer holes, good χ^2 of the fit, higher track momenta and more hits. Holes are positions in the particle trajectories with a sensitive detector element that is missing a hit. Inactive sensors or areal like edges on the silicon sensors, are not included in the definition of holes.

3.5 Simulation of proton-proton collisions

Theoretical models of the physics at the LHC must be compared to experimental results in order to investigate their validity. This is done using simulations of the proton-proton collisions created using the theoretical model of interest as reference. In the case of this thesis the physical theory of interest is the Standard Model since it is widely accepted as the most accurate available description of physics. The simulations are created using MC event generators that simulate the events in different steps.

This section first describes the steps of event generation, then continues with the simulated detector response before finally discussing track reconstruction.

3.5.1 Monte Carlo event generation

As mentioned in section 2.2, the phenomenology of pp collisions is complex and can involve many successive interactions between partons. Because of the complicated structure of the events they have to be simulated in several steps in order to produce accurate descriptions of the final particle states. MC event generators are used to simulate pp-collisions [37, 38]. The generators relevant for this work are

MadGraph5_aMC@NLO [39, 40] and **Powheg Box** [41, 42, 43].

The first step of event generation is Matrix element calculation where the user chooses a hard (high-momentum) primary interaction. The interaction is generated based on very precise matrix element calculations of the selected process. The event generator simulates the hard primary interactions using the available phase space and takes experimentally measured PDFs as input to determine the initial parton momenta. The result of this step is a short list of hard partons.

As a result of the accelerating colored partons present in the initial and final states, QCD radiation will be emitted and needs to be simulated. This is done by treating the ISR and FSR perturbatively, simulating a shower of quarks and gluons from the partons present in the initial and final states, causing the partons to lose energy in the process. This is known as the parton shower approach.

The phenomenology of fragmentation and hadron decay are described by the Lund string model [44].

The next step is detector simulation.

3.5.2 Detector simulation

In order to mimic the interaction between the simulated particles and the different parts of the detector, a simulated model of ATLAS is used. This model is implemented in the Geant4 [45] software. The model includes every active detector element and the surrounding magnetic field, and also other structures present such as support or electrical wiring. The Geant4 software simulates the interaction between the ATLAS model and the truth-level particles and calculates the energy deposited in every part of the detector. Any additional particles that appear as a consequence of these interactions are also added to the simulation.

Each of the subdetectors in ATLAS have had custom algorithms developed that turn the simulated energy deposits into hits in a process known as digitization, which is the next step in the MC event generation. The outcome of the digitization step is identical to the raw experimental read-out from the ATLAS detector.

The last step of the MC generation is reconstruction. Using the same methods as for experimentally obtained data, the digitized data can be reconstructed into particle data. This data is of the same type as real reconstructed data but with information about the true particles, called Truth particles.

3.6 Pileup simulation

Before the digitization step mentioned in Section 3.5.2, additional energy deposits of the so called pileup must be appended to the detector. There is both in-time and out-of-time pileup that both need to be simulated [46].

Minimum bias events refer to all possible hard scatter processes in the available phase space. Minimum bias events are simulated and used for in-time pileup and are then added as energy deposits in the detector simulation prior to digitization.

The in-time pileup is laid over the simulated hard-scatter events of interest based on experimentally obtained pileup distributions from a selected data-taking period. A distribution showing data from Run 2 can be seen in Figure 3.6. Minimum bias events are simulated based on these distributions and serve as pileup in the two MC samples discussed in this thesis. The out-of-time pileup affects the different detector instruments in different ways and any such effects need to be simulated accordingly.

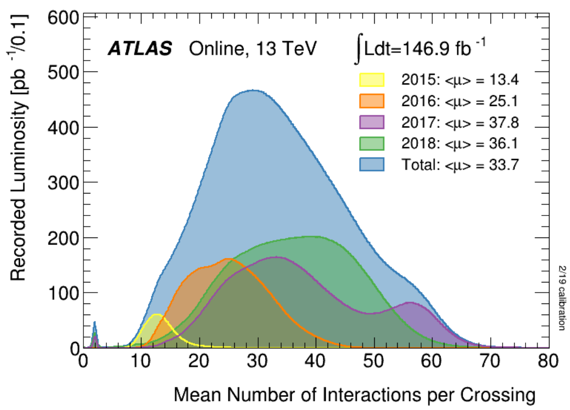

Figure 3.6: Mean number of interactions per BC recorded during Run 2 in the years 2015-2018 [47].

4 Luminosity measurement

4.1 Luminosity calibration

The multiple measurements from the different luminometers provide redundancy that is important for validation cross checks between the different systems. Based on Equation 3.4 the luminosity per bunch crossing can be expressed as

$$\mathcal{L}_b = \frac{f_r \epsilon \mu}{\epsilon \sigma_{inel}} = \frac{f_r \mu_{vis}}{\sigma_{vis}}, \tag{4.1}$$

where ϵ is the efficiency for the luminometer to record one inelastic pp interaction. μ_{vis} is the *visible interaction rate* given as the average number of pp interactions that the luminometer directly measures per bunch crossing and σ_{vis} is the *visible cross section* which is a calibration constant that is different for each luminometer and relates μ_{vis} to $\mathcal{L}_b$.

The visible cross section, σ_{vis}, is calibrated for each luminometer during special LHC fills where so called van der Meer (vdM) scans are performed. These special fills are low-μ fills, $< \mu > \sim 0.5$ [48], called vdM runs. During vdM runs there is zero crossing angle between the two colliding beams and large time separation (500 ns) between bunches.

To calibrate the visible cross sections, the beam sizes in the x- and y-directions are needed. To measure them, the beams are shifted away from from the nominal IP and scanned through each other separately in the x- and y-directions while measuring the detector counts. This allows for a measurement of the beam width.

The main ATLAS luminosity measurement is given by LUCID and calibrated in the vdM scans. Track counting is used for the calibration transfer and estimation of long term stability of the beam, described below, and is calibrated by normalizing the measurement to LUCID at low-μ. Track-counting is not calibrated in this way, but is instead normalized to low-μ LUCID measurements.

4.1.1 Calibration transfer and long term stability

The van der Meer (vdM) scans are performed under low-μ beam conditions and since the response of mainly LUCID does not rely linearly on μ [49], a calibration transfer from low to high μ becomes necessary. There is around a 10% increase in LUCID response when moving from $\mu \sim 0.5$ to $\mu \sim 40$.

A TC measurement is used to measure the non-linearity of the LUCID luminosity measurement. The TC measurement is done during a high-μ physics run where $< \mu >$ is changed over time and the calibration transfer to the low-μ vdM regime is then performed assuming no significant non-linear effects in the TC measurement.

The absolute LUCID luminosity scale is determined after performing the vdM calibration and applying the calibration transfer to higher luminosity. The performance of LUCID may drift over any data-taking period however, affecting the long term stability of the calibrations. To account for this, the LUCID luminosity measurements are controlled for every physics run by referencing measurements from other luminometers and keeping track of any discrepancies.

4.2 Track-counting

Track-counting is one of the many methods used to measure the luminosity in ATLAS. It is an integral part of the ATLAS luminosity measurement that is used to determine the long term stability of the beam as well as the calibration transfer, that were discussed in Section 4.1.1. Below are described the basic principles of track-counting and non-linear effects seen in previous ATLAS track-counting luminosity measurements [50].

4.2.1 Basic principles of track-counting

There is a linear relationship between the number of tracks and the number of interactions per BC. Track-counting is based on this relationship and determines the luminosity by measuring the average number of tracks selected with specific *selection criteria* called Working Points, described in further detail in Section 5.1.

Once tracks have been reconstructed, as described in section 3.4, they need to pass certain selection criteria to ensure that the track quality is acceptable. The earliest of these selection criteria are based on the standard ATLAS track reconstruction WP, called *TightPrimary*, which was designed by the ATLAS tracking Combined Performance group [51]. The selection criteria for *TightPrimary* can be seen in Table 4.1.

Table 4.1: Selection criteria applied for the TightPrimary selection. N^{Pix}_{hits} and N^{SCT}_{hits} are the total number of hits in the Pixel detector and the total number of hits in the SCT detectors, respectively. N^{Pix}_{Dead} and N^{SCT}_{Dead} denote the number of inactive sensors the Pixel and SCT detectors, respectively. N^{IBL}_{hits} and $N^{B-layer}_{hits}$ are the total number of hits in the IBL and hits in the first layer of the Pixel detector, respectively. N^{SCT}_{holes} and N^{Pix}_{holes} denote the number of holes in the SCT and Pixel detectors, respectively. N^{SCT}_{shared} and N^{Pix}_{shared} are the number of shared single-sided hits in the SCT detector and shared hits in the Pixel detector, respectively.

Criterion	**TightPrimary**
p_T	≥ 500 MeV
$\mid \eta \mid$	<2.5
$N^{Si}_{hits} = N^{Pix}_{hits} + N^{Pix}_{Dead} + N^{SCT}_{hits} + N^{SCT}_{Dead}$	≥ 9 if $\mid \eta \mid \leq 1.65$, ≥ 11 if $\mid \eta \mid > 1.65$
$N^{IBL}_{hits} + N^{B-layer}_{hits}$	>0 if hits are expected in both layers
N^{Pix}_{holes}	$= 0$
N^{SCT}_{holes}	≤ 2
$N^{Pix}_{shared} + \frac{1}{2} N^{SCT}_{shared}$	≤ 1

As stated above, there is in theory a linear relationship between the average number of tracks and the number of inelastic *pp* interactions, $\langle\mu\rangle$, per bunch crossing. But because of non-ideal detector efficiencies and fake tracks, a non-linear relationship is observed in experiment.

After this step, stricter requirements from additional WPs can be applied before the track-counting measurement in order to reduce the number of fake tracks, see 4.2.1, while at the same time retaining high efficiency. Many different WPs are tested in order to find the best performing selection.

The number of tracks per event is a function of μ and can be expressed as:

$$N_{trk}(\mu) = N_{trk}^{true}(\mu) \cdot \epsilon_{r\times s}(\mu) + N_{trk}^{fake}(\mu), \tag{4.2}$$

where $N_{trk}^{true}(\mu)$ (or $N_{trk}^{fake}(\mu)$) is the number of true (or fake) tracks per event and $\epsilon_{r\times s}(\mu)$ is the μ-dependent track reconstruction times selection efficiency. For an efficiency of 1 and a fake rate of 0, the track-counting measurement is perfectly linear with μ. The goal of the work described in this thesis is to investigate how well this holds in reality. In data, the exact μ-value is not known a priori, which is why this investigation is performed in MC simulation.

Fake tracks are the result of falsely reconstructed tracks that could have formed due to combination of unrelated hits. It is assumed that the rate of fake tracks at lower pileup values should be lower because of the fact there are fewer hits in the detector, making it easier for the track reconstruction algorithms to determine the true particle trajectories. There is a decreased tracking efficiency at high μ due to detector saturation which is not a problem at lower μ-values. The effect of fake tracks are assumed to be negligible below $\mu = 20$ for these studies.

The average number of tracks is expected to go linearly with μ but the track selection and reconstruction efficiency as well as the number of fake tracks in Equation 4.2 both have a non-linear dependence on μ that affect the track-counting luminosity measurement. The uncertainty on the luminosity is the biggest obstacle for high-precision measurements at ATLAS such as background estimations in searches for new physics and in cross-section measurements which rely on the precision of the measured integrated luminosity.

5 Working points and sample validation

This thesis studies the non-linear effects in the track-counting measurement using two different sets of samples containing MC generated events. One of the main differences between the two sets lies in the choice of hard scattering interaction. The first set is simulated with $Z \to \mu\mu$ as the chosen hard interaction. 2.4 million simulated events are used from this set which is 10% of the total number of simulated events. The second set is simulated using a single neutrino particle gun (SNPG), where a single neutrino fired through the detector is the hard interaction. 1.8 million simulated events are used from this set which is 10% of the total number of simulated events. These samples need to be validated before they can be used for the TC luminosity measurement.

The two MC generated samples considered in this thesis use hits from different ATLAS subdetectors for reconstructing the tracks. The $Z \to \mu\mu$ sample reconstructs tracks using special settings, which are also used to reconstruct tracks in data for the track-counting measurement, called *VtxLumi* settings, that uses hits from the IBL, Pixel and SCT detectors. The single neutrino sample tracks are instead reconstructed using standard track reconstruction which in addition to the IBL, Pixel and SCT detectors uses the TRT. Other differences between the two reconstruction methods include differing minimum p_T requirements (500 MeV for standard reconstruction and 900 MeV for VtxLumi) as well as a different number of allowed consecutive holes per track candidate (2 in standard reconstruction and 1 with VtxLumi), although the impact of the latter is considered to be small. See Table 5.1 for more details on the samples.

Table 5.1: Information about the $Z \to \mu\mu$ and SNPG MC samples. The release numbers refer to the Athena release that was used to construct the samples [52], the hard scatter interaction is the most energetic interaction in the generated events and both μ-distributions have a flat profile and is simulated between the given μ-values ($Z \to \mu\mu$: 0-100, SNPG: 0-80). See text for more information about the reconstructions.

	Z$\to \mu\mu$ sample	**SNPG sample**
Release	R21	R22 (22.0.41.3)
Hard scatter interaction	$Z \to \mu\mu$	Single neutrino particle gun
μ-distribution	Flat μ, 0-100	Flat μ, 0-80
Reconstruction	VtxLumi	Standard track reconstruction

A flat μ-profile refers to the fact that an equal amount of events are generated at each μ-value in the samples. A flat profile ensures that enough statistics are available at all values of μ which is important for the studies presented in this thesis.

This section will describe the different WPs that were used during LHC Run 2 and the new WPs proposed for Run 3. Then follows a brief description of the structure of the MC data samples and assessment of the $Z \to \mu\mu$ and SNPG MC samples.

5.1 Working Points

After track reconstruction, the tracks that are to be used in the luminosity measurement need to pass a number of selection criteria in order to ensure good track quality. The tracks already fulfill the criteria that were applied during track reconstruction, but are further constrained by the *TightPrimary* WP, which requires tracks to pass the criteria listed in Table 4.1.

The uncertainty on the track-counting luminosity measurement is dependent on the choice of Working point, which is the main reason to study multiple different ones.

During LHC Run 2 a number of additional WPs were created, based on the *TightPrimary* WP. The ones studied in this thesis are

- *Tight* (*T*),
- *TightLumi* (*TL*),
- *TightModLumi* (*TML*)
- and *TightModSiPlusLumi* (*TMSPL*).

The selection criteria for these WPs are seen in Table 5.2. The WPs all require a minimum track p_T of 900 MeV. The T WP is identical to the standard track reconstruction requirements with the only difference being the higher p_T criteria. On the *TML* and *TMSPL* WPs there is a tightened $\mid \eta \mid$ requirement and an allowance for one Pixel hole. *TL*, *TML* and *TMSPL* all have a requirement on the minimum d_0-significance which is introduced to decrease the number of fake tracks. Finally there is a minimum requirement of 9 and 10 Silicon hits for *TML* and *TMSPL* respectively, with hits being accepted in the full η-range.

Table 5.2: Selection criteria for the WPs created for LHC Run 2 that are studied in this thesis. All WPs have a track p_T requirement of ≥900 MeV. The criteria in blue are identical to the criteria given by *TightPrimary*.

Criterion	Tight	TightLumi	TightModLumi	TightModSiPlusLumi
$\mid \eta \mid$	<2.5	<2.5	<1.0	<1.0
N^{Si}_{hits}	≥ 9 if $\mid \eta \mid \leq 1.65$ else ≥ 11	≥ 9 if $\mid \eta \mid \leq 1.65$ else ≥ 11	≥ 9	≥ 10
N^{Pix}_{holes}	$=0$	$=0$	≤ 1	≤ 1
$\mid d_0 \mid / \sigma_{d_0}$	-	<7	<7	<7

An advantage of studying multiple WPs is that they can be compared to eachother. The selections have different fake track rates and track selection efficiencies and can therefore be used for different purposes. *TML* was the nominal WP used for the track-counting measurement in Run 2, and the other WPs were used for studying systematic uncertainties and the long term stability of beams.

Four new WPs introduced in response to the expected increase of luminosity in LHC Run 3 are also studied. These are called

- *TightModFullEtaLumi* (*TMFEL*),
- *TightModHighPtStrictLumi* (*TMHPSL*),
- *TightModFullEtaHighPtStrictLumi* (*TMFEHPSL*)
- and *TightModSiPlusHighPtStrictLumi* (*TMSPHPSL*)

and their respective selection criteria are listed in Table 5.3.

Table 5.3: Selection criteria for the new WPs created for LHC Run 3.

Criterion	**TightModFullEtaLumi**	**TightModHighPtStrictLumi**	**TightModFullEtaHighPtStrictLumi**	**TightModSiPlusHighPtStrictLumi**
p_T	>0.9 GeV	>1.0 GeV	>1.0 GeV	>1.0 GeV
$\mid \eta \mid$	<2.5	<1.0	<2.5	<1.0
N^{Si}_{hits}	≥ 9 if $\mid \eta \mid \leq 1.65$ else ≥ 11	≥ 9	≥ 9 if $\mid \eta \mid \leq 1.65$ else ≥ 11	≥ 10
N^{Pix}_{holes}	≤ 1	≤ 1	≤ 1	≤ 1
$\mid d_0 \mid / \sigma_{d_0}$	<7	<5	<5	<5

TMFEL has selection criteria similar to the Run 2 nominal WP, *TML*, only with a looser $\mid \eta \mid$ requirement and stricter restrictions on N^{Si}_{hits}. The remaining three WPs, *TMHPSL*, *TMFEHPSL* and *TMSPHPSL*, all put tighter restrictions on d_0-significance and require a track p_T above 1 GeV. *TMHPSL* and *TMSPHPSL* require 9 respective 10 Silicon hits and both WPs require $\mid \eta \mid$ strictly less than 1. All WPs allow up to one Pixel hole.

A program (written by the author) based on these WPs sorts through all tracks in the reconstructed events and filters them based on the selection criteria. The tracks that pass the selection criteria of the WPs are used for the track-counting luminosity measurement. The computational framework used for this task is the Service for Web based ANalysis (SWAN), provided by CERN. All code is written in Python.

5.2 Validation of simulated samples

The work described in this thesis is carried out with data stored in a standard data format used for all track-counting MC studies in ATLAS. This corresponds to ROOT-files with records about the track parameters as well as a boolean for each Run 2 WP (*T*, *TL*, *TML*, *TMSPL*) which is true if the track passes the corresponding requirements.

The two samples that are to be used in the following analysis, the $Z \rightarrow \mu\mu$ sample and the SNPG sample, are not created by the author and must thus be assessed before the analysis. For these studies, $2.8 \cdot 10^6$ MC generated events are used for the $Z \to \mu\mu$ sample and $1.8 \cdot 10^6$ events for the SNPG sample.

Before starting with the track-counting studies, some tests are carried out with a small fraction of events from the given MC generated samples.

5.2.1 Track parameters

The WPs require some of the track parameters to meet certain selection criteria, given in Tables 5.2 and 5.3. To control that these requirements are fulfilled by each of the WPs, the track distributions of these parameters are plotted.

Figure 5.1 shows the transverse momenta of the tracks. It can be seen that tracks belonging to *TMHPSL*, *TMFEHPSL* and *TightModSiPlusHighPtStrictLumi* all have a p_T greater than 1 GeV while the tracks from the other WPs begin at 0.9 GeV in agreement with the track selection criteria.

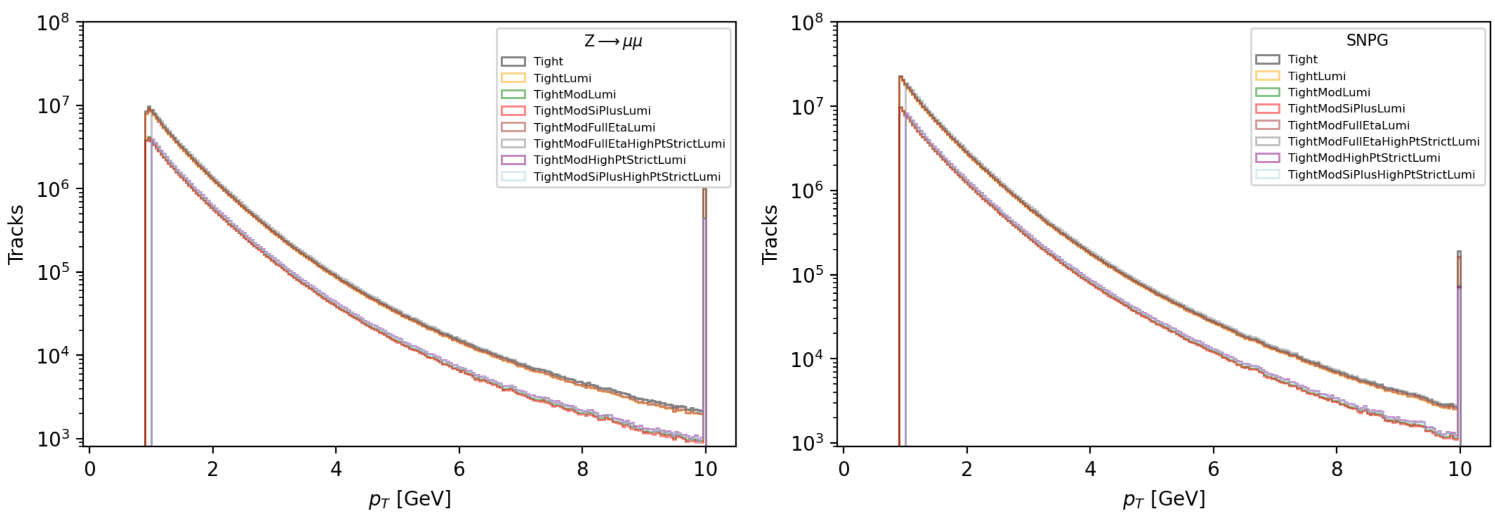

Figure 5.1: Track distributions of the track momenta for the $Z \to \mu\mu$ (left) and SNPG (right) samples with overflow bins at 10 GeV.

Figure 5.2 shows the track η-distributions for the two samples. Four of the WPs (*TML*, *TMSPL*, *TMHPSL* and *TMSPHPSL*) are restricted to $|\eta| < 1$ while the other four WPs have an acceptance of $|\eta| < 2.5$. This is clearly seen in the figures.

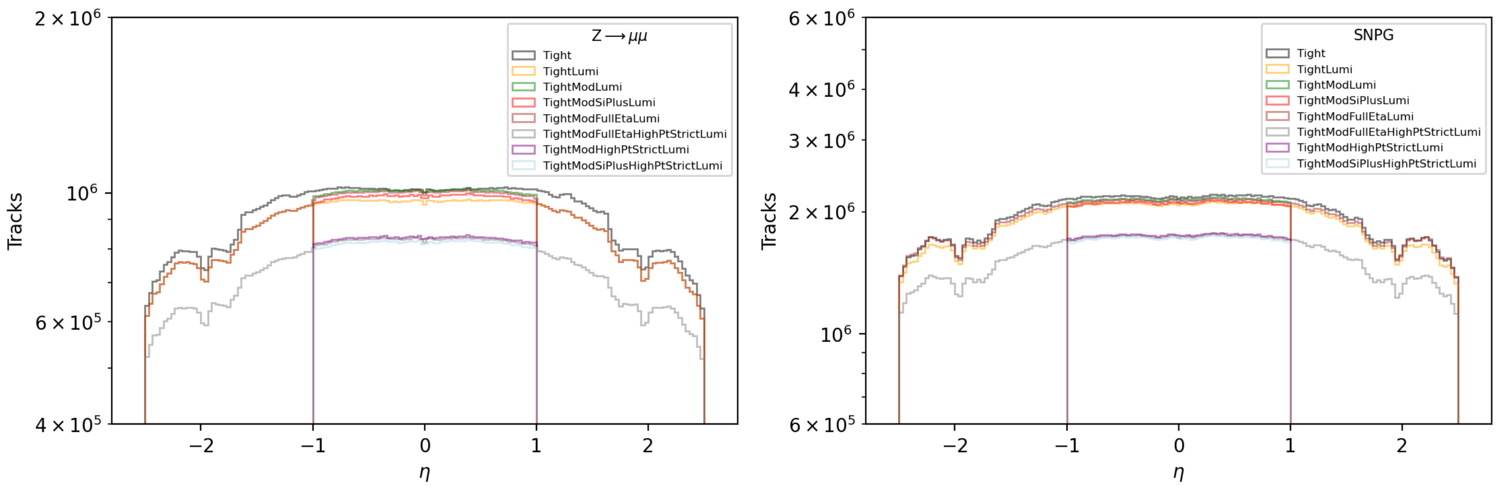

Figure 5.2: Track distributions of the parameter η for the $Z \to \mu\mu$ (left) and SNPG (right) samples.

Figures 5.3 and 5.4 show the number of silicon hits for all the WPs for both samples. The Run 2 and Run 3 WPs are shown separately for a more detailed view. The requirement on *TMSPL* and *TMSPHPSL* of at least 10 silicon hits can be seen in the figures.

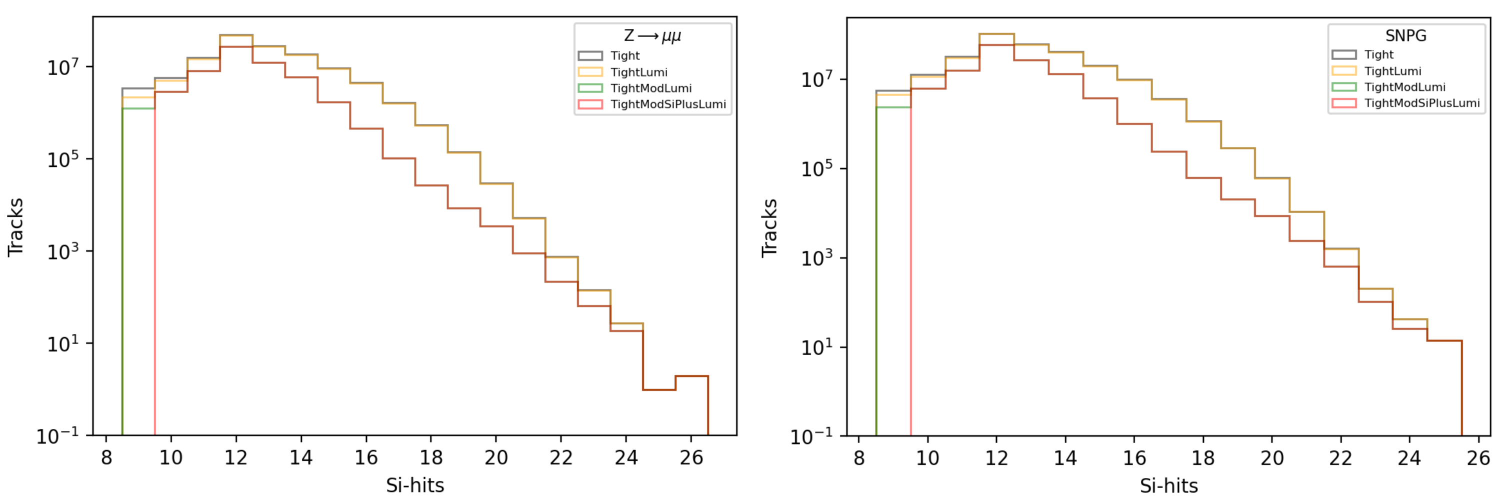

Figure 5.3: Track distributions of the number of Silicon hits for the Run 2 WPs, shown for the $Z \to \mu\mu$ (left) and SNPG (right) samples.

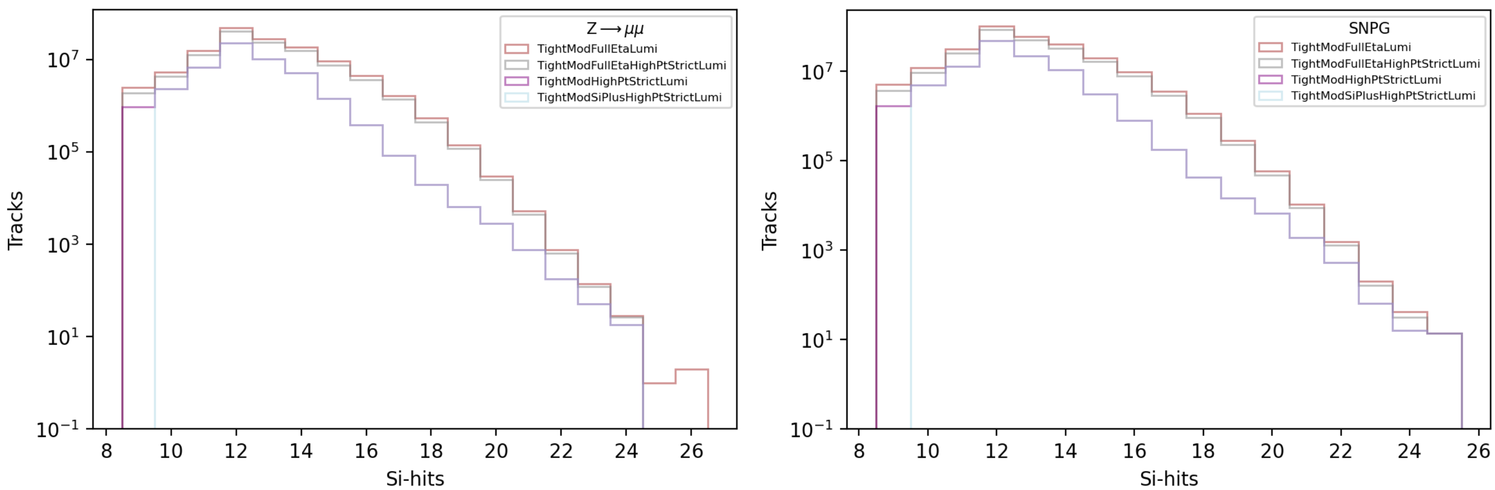

Figure 5.4: Track distributions of the number of Silicon hits for the Run 3 WPs, shown for the $Z \rightarrow \mu\mu$ (left) and SNPG (right) samples.

The *Tight* and *TightLumi* WPs accept zero pixel holes while the rest of the WPs accept up to 1 pixel hole. Figure 5.5 show the number of Pixel holes for the different WPs in the two samples and Figure 5.6 shows *Tight* and *TightLumi* separately to show that the tracks accepted by these WPs are restricted to $N_{holes}^{Pix} = 0$ as per their selection criteria.

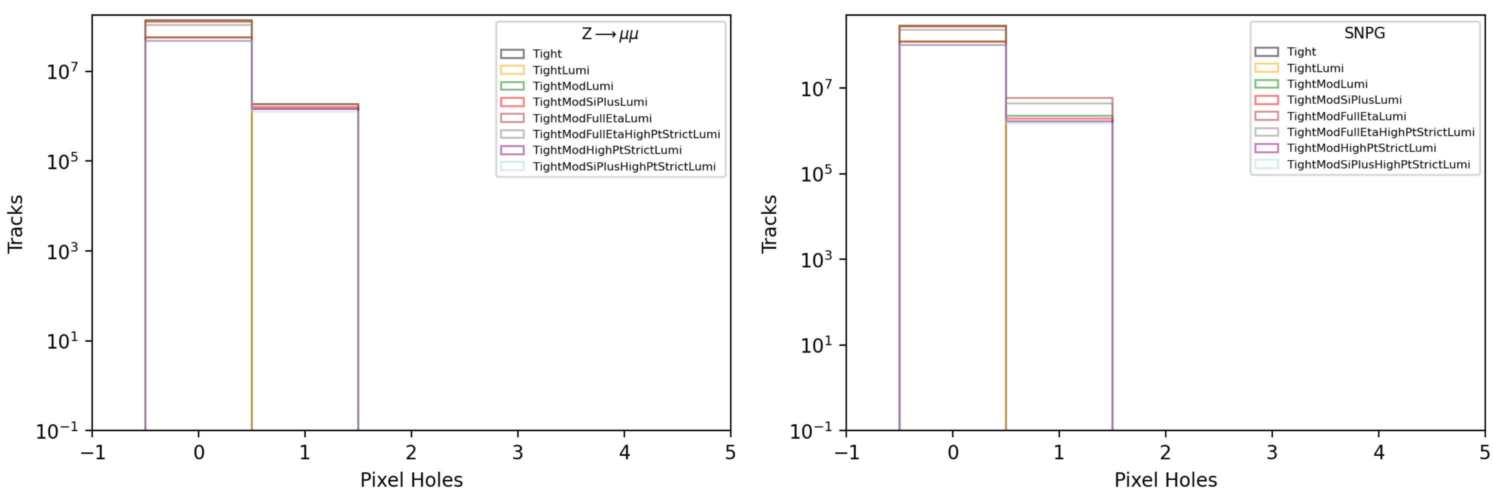

Figure 5.5: Track distributions of the number of Pixel holes for the $Z \rightarrow \mu\mu$ (left) and SNPG (right) samples.

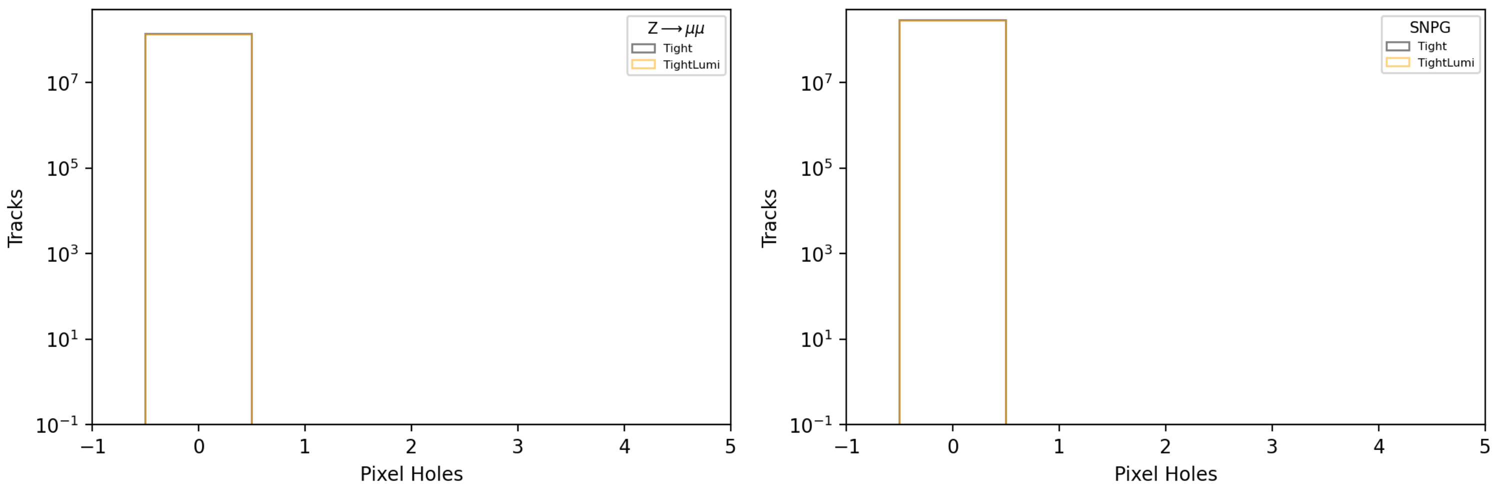

Figure 5.6: Track distributions of the number of Pixel holes for the WPs *Tight* and *TightLumi*, shown for the $Z \to \mu\mu$ (left) and SNPG (right) samples. The tracks accepted by these WPs are restricted to $N_{holes}^{Pix} = 0$ as per their selection criteria. *Tight* accepts more tracks than *TightLumi* although this is not clear by the figure.

The final selection criterion is d_0-significance on the tracks which is shown in Figure 5.7. T has no requirement on the d_0-sign. and is spread out accordingly in the figure. TL, TML, $TMSPL$ and $TMFEL$ all require a d_0-sign. below 7, while the remaining WPs require a d_0-sign. less than 5. The figure shows that these requirements are all met. It can also be seen that the WPs with wider η-acceptance (T, TL, $TMFEL$ and $TMFEHPSL$) accept more tracks. The track distribution of T is lower because it is unbounded by d_0-significance.

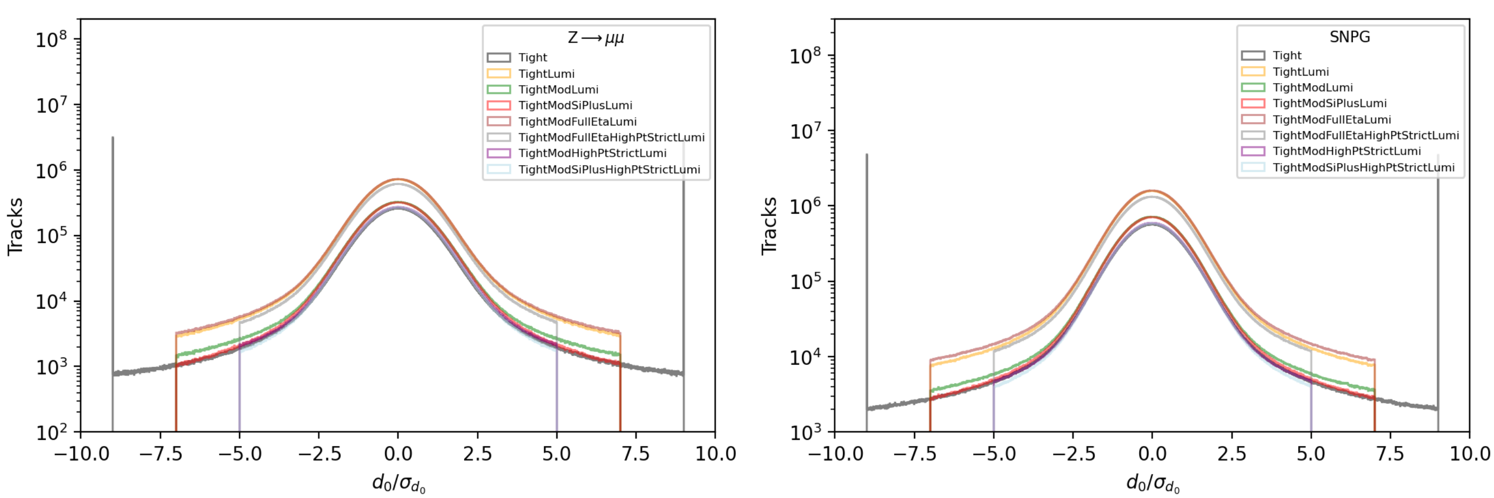

Figure 5.7: Track distributions of the parameter d_0-significance for the $Z \to \mu\mu$ (left) and SNPG (right) samples, with overflow bins at ± 9.

All track parameter distributions look as expected. Each WP is observed to meet their respective selection criteria.

5.2.2 Pileup profile

As previously mentioned, the μ-profiles of the MC generated samples are expected to be completely flat when using the full set of MC generated samples. Only ~10% of the full set of MC generated samples were available for these studies, so slight fluctuations from a flat μ-profile are to be expected and can be seen in Figure 5.8.

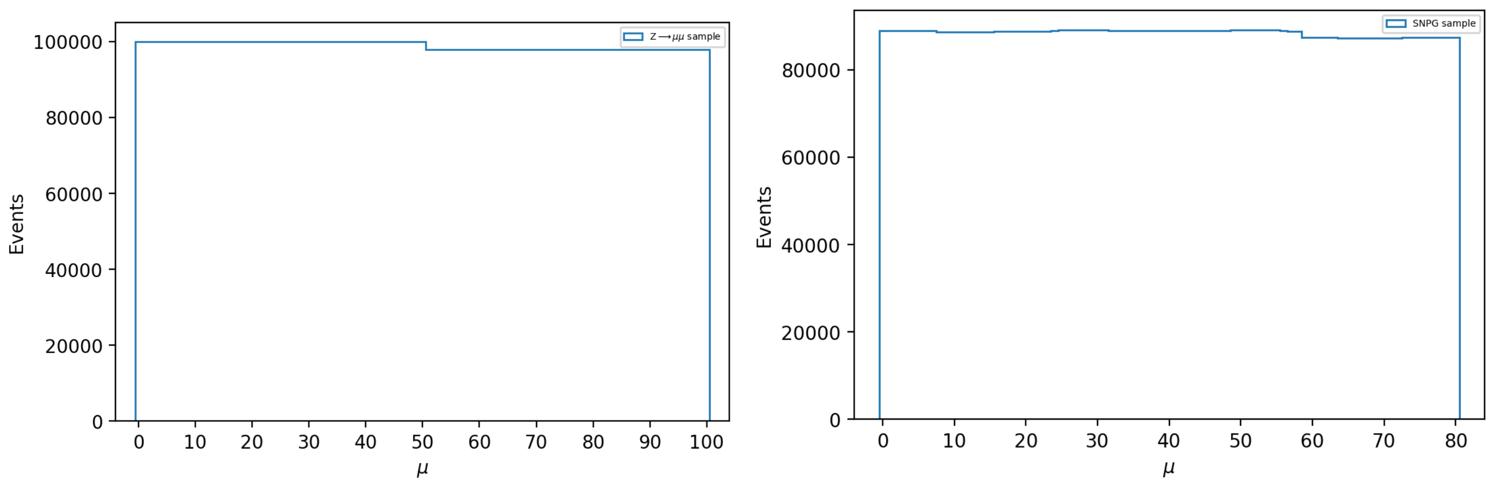

Figure 5.8: The number MC generated events of the $Z \to \mu\mu$ sample (left) and the SNPG sample (right) using all available MC samples. Both samples show the expected flat distribution with only slight fluctuations (±1%).

It is worth noting that fluctuations will not affect the TC luminosity measurement as long as the event sample size is large enough at each value of μ. This is because the quantity of interest in the TC measurement is the average number of tracks per event, thus only the uncertainty of the measurement will be affected by fluctuations from a flat profile.

The number of hard scatter interactions in both samples are expected to be equal to one for all events. From Figure 5.9 it is clear to see that this is the case in both samples.

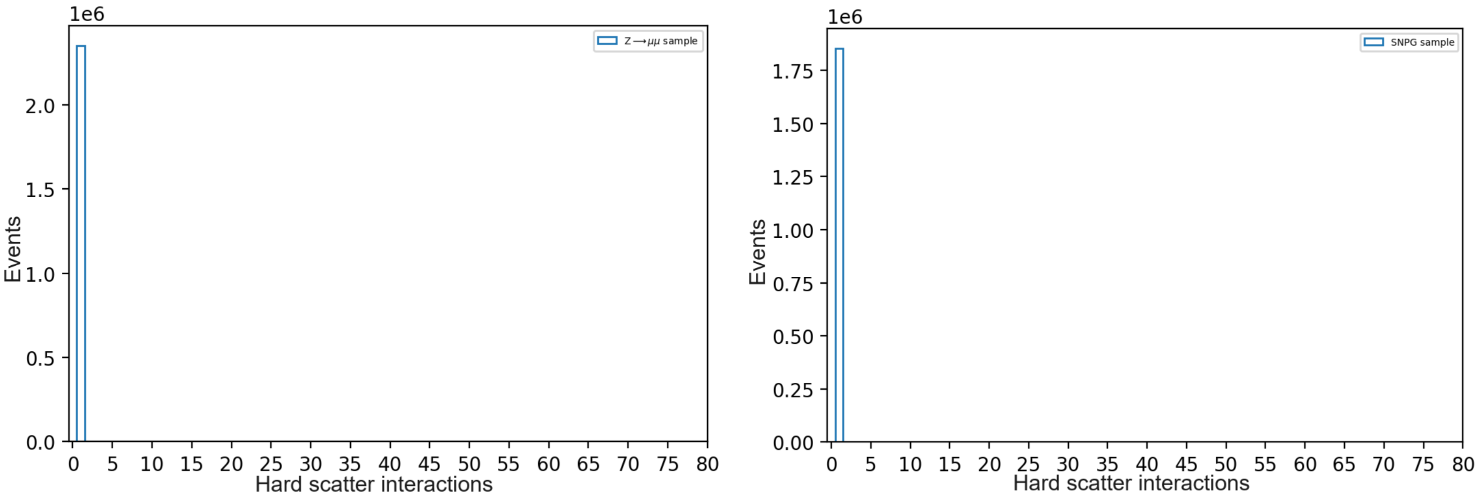

Figure 5.9: The number of hard scatter interactions in the $Z \to \mu\mu$ (left) and the SNPG (right) in all events. Both samples show one interaction for every event.

Next, the distribution of the number of pileup interactions in the events are plotted for both samples and can be seen in Figure 5.10. The number of interactions are distributed as expected, with a smooth distribution of events and a tail of events which is strictly dying off at pileup levels corresponding to the largest simulated μ-values for respective sample. The main contribution to the peaks at zero interactions comes from the events at $\mu = 0$, where all events result in zero pileup interactions. This event concentration at $\mu = 0$ also explains the slight dip in events at 1 pileup interaction where only events of $\mu \geq 1$ contribute.

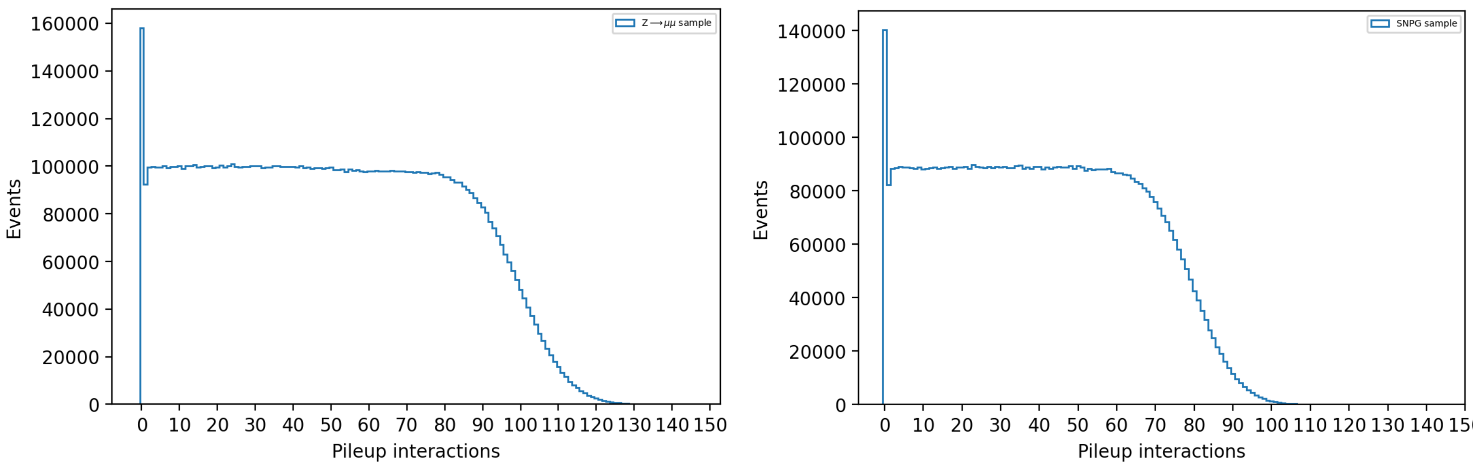

Figure 5.10: The number of pileup interactions for both the $Z \rightarrow \mu\mu$ sample (left) and the SNPG sample (right).

Finally, the distribution of the number of tracks produced per event at different values of μ are checked. In Figure 5.11 the normalized number of tracks for $\mu = 5, 10, 20, 50, 80$ are shown. The WP *TML* was used for this check simply for the reason that it was the WP recommended to use during Run 2, but choice of WP has no bigger significance.

The mean number of produced tracks per event is expected to be greater than the number of pileup interactions in the event because of the many interactions following the initial collisions. The track distributions are thus expected to have a mean above the corresponding μ-value. The distributions are also expected to include some events for which the number of tracks are lower or equal to their corresponding μ-value, since there are events for which many tracks are not reconstructed or do not meet the required selection criteria.

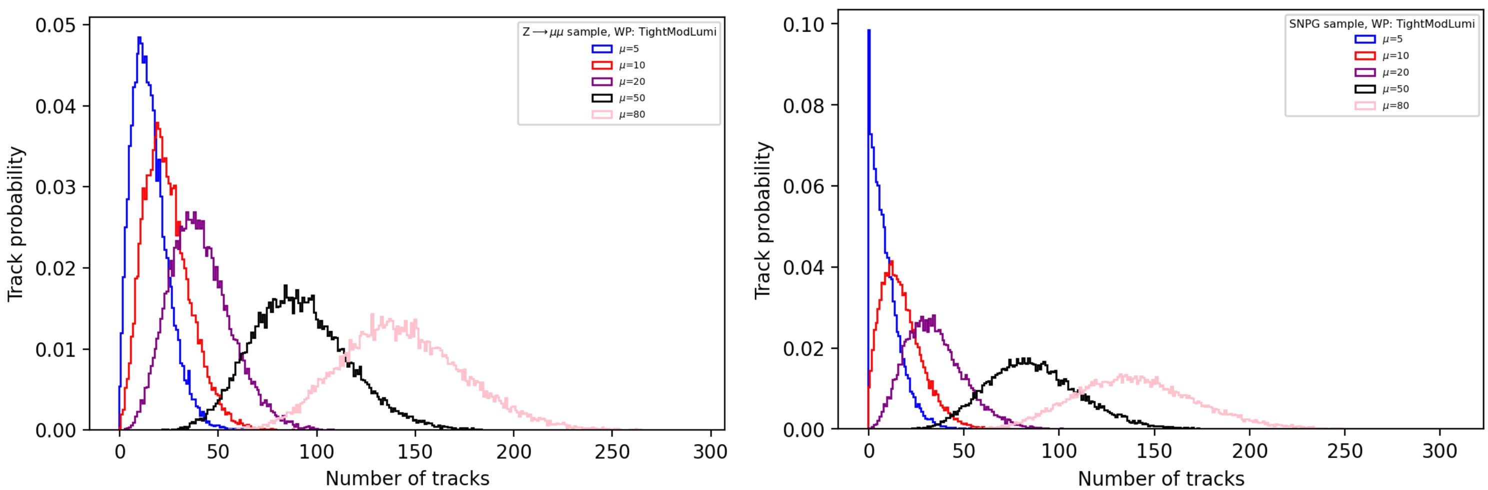

Figure 5.11: The distribution of N_{trk} for the $Z \to \mu\mu$ sample (left) and SNPG sample (right) at $\mu = 5, 10, 20, 50, 80$

Also interesting to note is the differences in the distributions of the number of tracks at $\mu = 1$ for the two samples, which is shown in Figure 5.12 below. More tracks are present in the $Z \to \mu\mu$-sample, likely due to the constributions of the physical hard scatter.

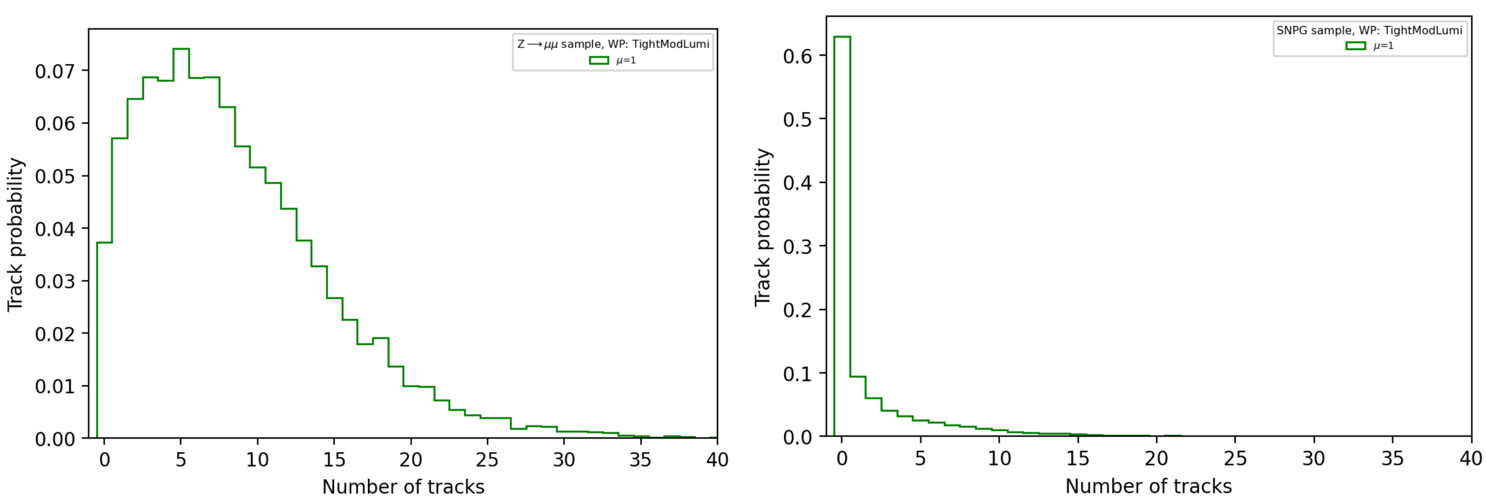

Figure 5.12: The distribution of N_{trk} for the $Z \to \mu\mu$ sample (left) and SNPG sample (right) at $\mu = 1$.

6 Track-counting luminosity measurement

The linear relationship between the average number of tracks, $< N_{trk} >$, and μ allows for the luminosity to be inferred simply by $< N_{trk} >$. But as was seen in Section 5.2.2 there are differences between the sets of MC generated events, and these differences will affect the track-counting.

6.1 Sample selection

At zero pileup, $\mu = 0$, the number of expected tracks is zero. However because the MC event generation requires a hard-scatter interaction to be present in all events this is not the case if the chosen hard-scatter interaction involves particles that are visible to the detector. This is the case for the MC generated events that use the hard-scatter interaction $Z \rightarrow \mu\mu$. As can be seen in left histogram in Figure 6.1 there is a non-zero probability for tracks to be detected at $\mu = 0$ because of the chosen hard-scatter interaction.

When instead choosing a SNPG to generate hard-scatter events in the MC generation no tracks from the hard-scatter are detected by the ID since no charged particles are present, see the right histogram in Figure 6.1. This approach solves the problem of tracks from the hard-scatter interaction being present in every event and produces simulated events that more closely match experimental results.

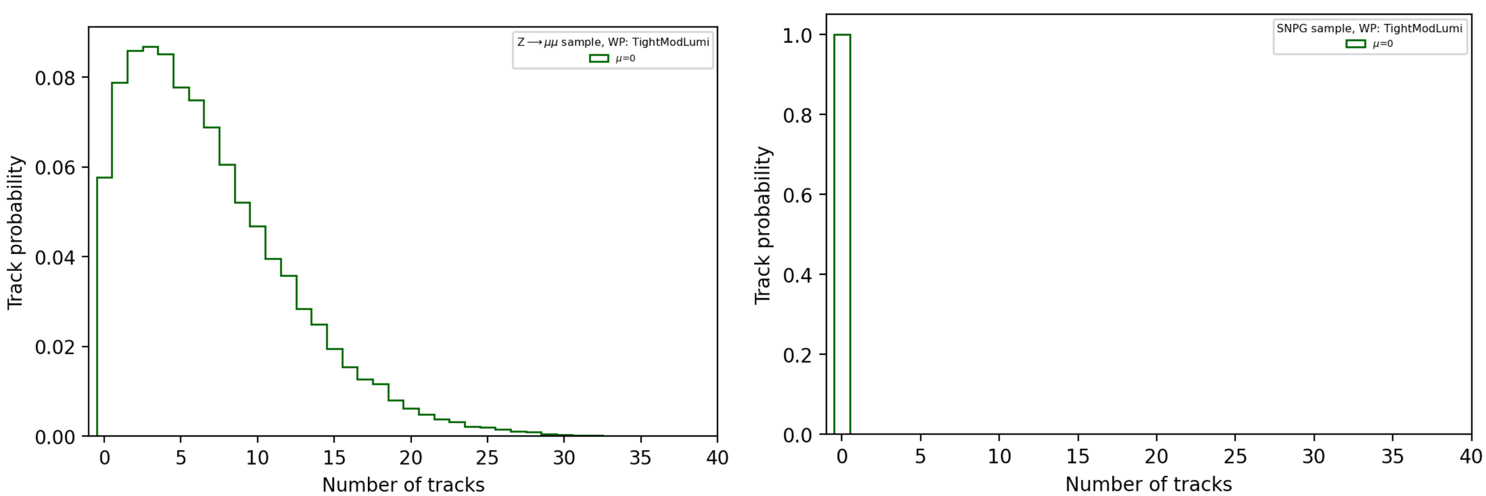

Figure 6.1: Normalized distributions of N_{trk} for the $Z \rightarrow \mu\mu$ sample (left) and SNPG sample (right) at $\mu = 0$.

In the $Z \rightarrow \mu\mu$ sample, $\sim 94\%$ of tracks are accepted by the *TML* WP while no tracks are accepted by the SNPG sample as can be seen in the figures. The presence of tracks coming from the hard scatter will affect the track-counting luminosity measurement.

This can also be seen by looking at the average number of tracks as a function of μ, which will be done during the TC luminosity measurement. Figure 6.2 shows that none of the trends start at zero at $\mu = 0$ in the $Z \to \mu\mu$ sample, which is simply not physical since no tracks should be seen if no particle interactions take place.

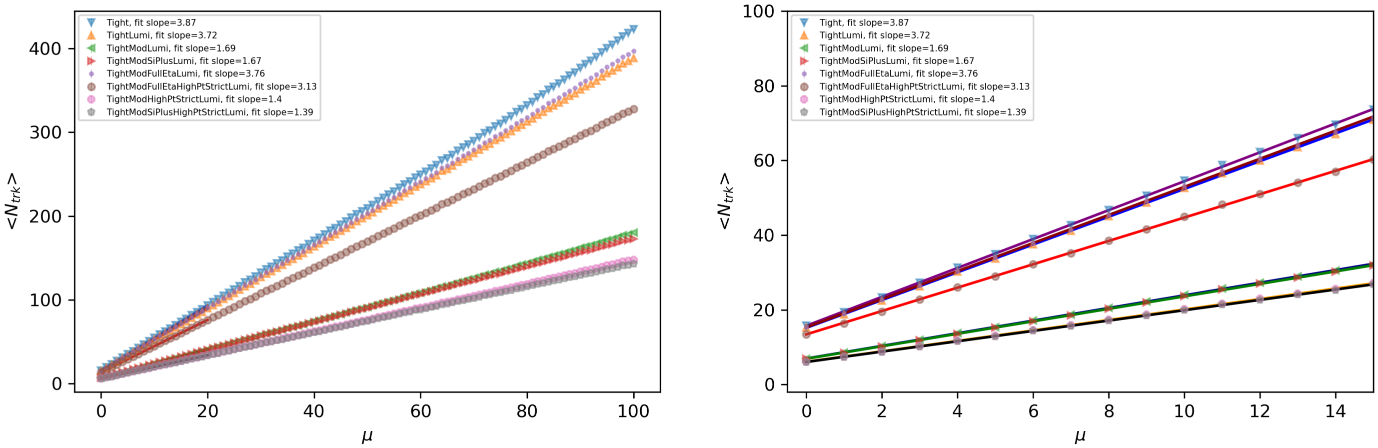

Figure 6.2: The average number of tracks as a function of μ for all WPs shown for the $Z \to \mu\mu$ sample (left) and the same zoomed in around smaller values of μ (right). The average number of tracks at $\mu = 0$ is non-zero for all WPs.

Advantages of having no track contribution from the primary interactions are that track-counting becomes straightforward with only pileup to consider as well as producing results that more closely resemble experiment. The set of samples that should be used for the track-counting luminosity measurement is the SNPG set. Because of the reasons mentioned above the $Z \to \mu\mu$ set will not be considered in Sections 6.2 and 6.3.

6.2 Linearity of the track-counting luminosity measurement

As discussed in Section 6.1, the MC sample that should be used for the track-counting measurement is the SNPG sample. What follows in this section are results from analysis of the SNPG sample.

Figure 6.3 shows the average number of tracks as a function of μ for the Run 2 WPs. Linear fits are made between $\mu = 0$ and $\mu = 20$ where it is assumed that no non-linear effects are present in the data. The slopes of the linear fits are seen for each of the WPs in the figure and their steepness indicate the calibration constant that is needed to convert N_{trk} to μ, but are otherwise arbitrary.

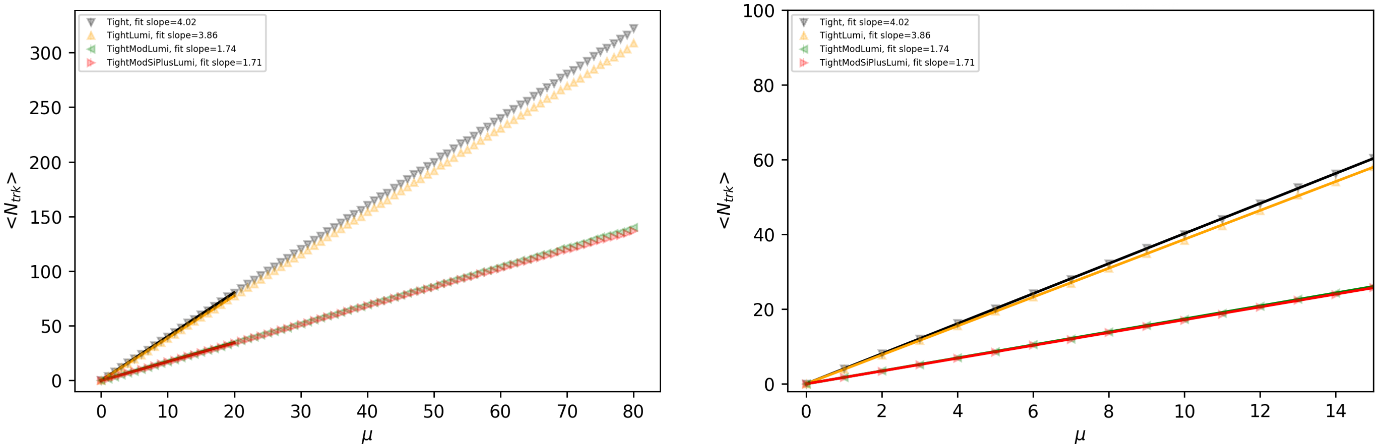

Figure 6.3: Average number of tracks as a function of μ for the Run 2 WPs for the SNPG sample (left) and the same zoomed in around smaller values of μ (right). The average number of tracks is zero at $\mu = 0$ for all WPs as expected. The steepness of the slopes indicate the calibration constant that is needed to convert N_{trk} to μ, but is otherwise arbitrary.

Figure 6.4 shows the average number of tracks as a function of μ for the new Run 3 WPs. Linear fits are made between $\mu = 0$ and $\mu = 20$ where it is assumed that no non-linear effects are present in the data. This assumption would have to be verified by looking at the fake track rate. The slopes of the linear fits are seen for each of the WPs in the figure.

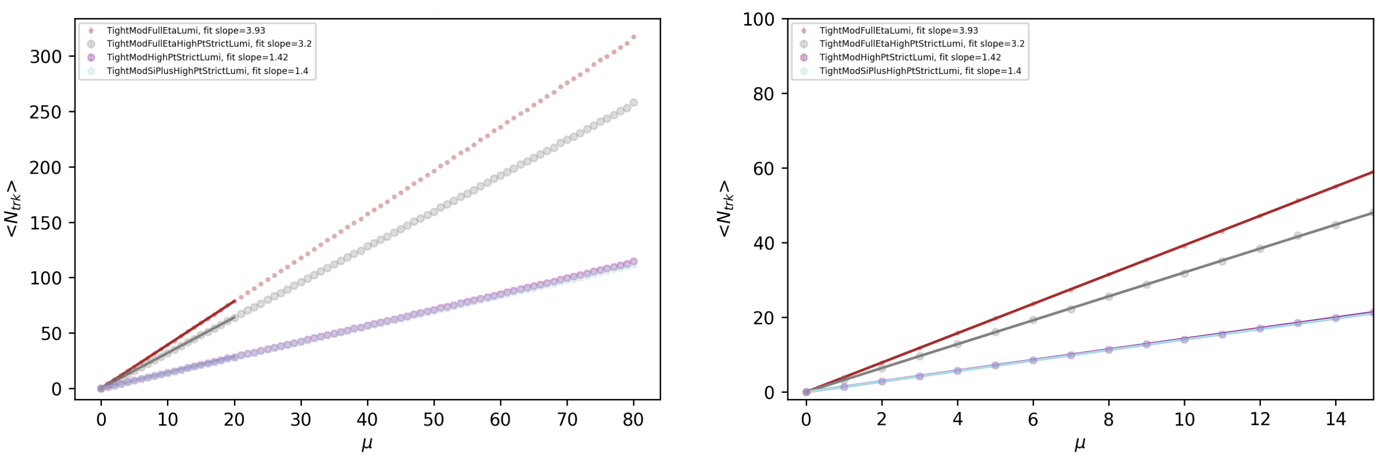

Figure 6.4: Average number of tracks as a function of μ for the Run 3 WPs for the SNPG sample (left) and the same zoomed in around smaller values of μ (right). The he average number of tracks is zero at $\mu = 0$ for all WPs as expected. The steepness of the slopes indicate the calibration constant that is needed to convert N_{trk} to μ, but is otherwise arbitrary.

In Figure 6.5 the average number of tracks as a function of μ are shown for all WPs. It is difficult to say anything about the linearity of the μ-dependence from these plots but the slopes give insight into the efficiencies of the different WPs. From the values of the slopes it can be seen that the T WP accepts the most number of tracks which is to be expected since T has the loosest selection requirements out of the WPs. The WPs with the highest η acceptances are T, TL, $TMFEL$ and $TMFEHPSL$, see Tables 5.2 and 5.3, these are also the WPs with the steepest slopes. The only difference between T and TL is the added d_0-significance requirement on the latter, which results in slightly fewer tracks being accepted by TL. TML differs from TL in that it has a lower η acceptance range and allows for up to one pixel hole per track. $TMSPL$ is identical to TML except for the stricter requirement of at least 10 silicon hits. $TMFEL$ has the same requirements as TML (with the same restrictions on N_{hits}^{Si} as *TightPrimary*) except for the relaxed η requirement. $TMFEHPSL$ accepts fewer tracks than $TMFEL$ due to the stricter p_T and d_0 significance criterion. $TMHPSL$ is identical to $TMFEHPSL$ but with a lower η acceptance, which lowers the accepted number of tracks significantly. $TMSPHPSL$ is almost identical to $TMFEHPSL$ only requiring one more silicon hit. This results in $TMSPHPSL$ being the WP that accepts the lowest (mean) amount of tracks out of all the WPs.

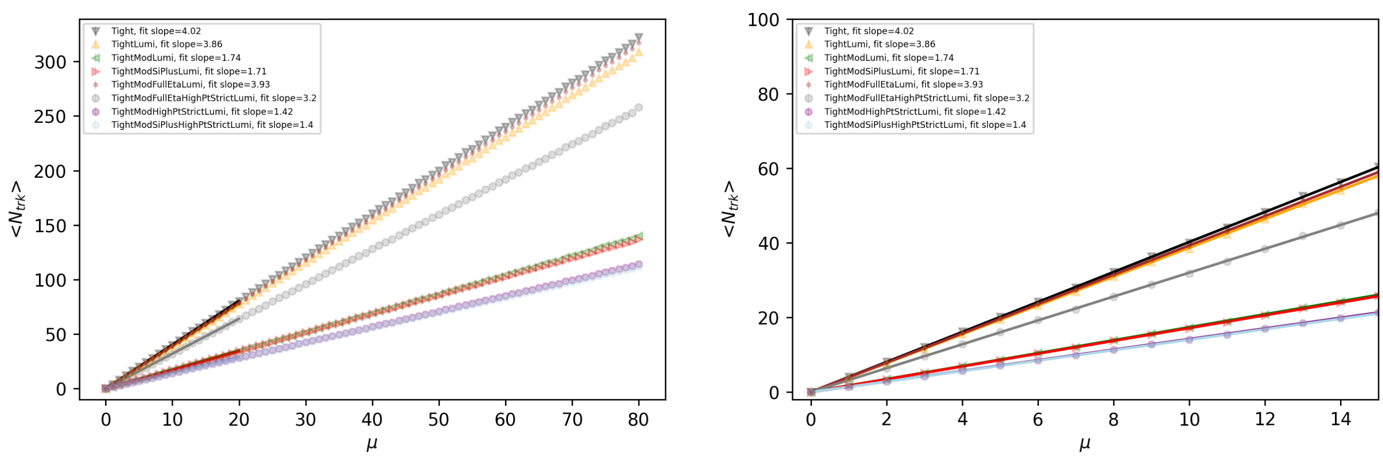

Figure 6.5: Average number of tracks as a function of μ for the all WPs for the SNPG sample (left) and the same zoomed in around smaller values of μ (right). The average number of tracks is zero at $\mu = 0$ for all WPs as expected. The steepness of the slopes indicate the calibration constant that is needed to convert N_{trk} to μ, but is otherwise arbitrary.

6.3 Non-linear effects

As discussed in Section 4.2.1, both the track reconstruction times selection efficiency and the number of fake tracks depend non-linearly on μ and contribute to non-linear effects in the track-counting luminosity measurement. To see the non-linear effects more clearly, each of the WPs in Figure 6.5 are compared to their respective linear fit so that any non-linearities become appearent. The figures in 6.6 show the ratios of the average number of tracks, $< N_{trk}(\mu) >$, and the linear fits for all WPs.

The figure shows that the statistical uncertainty is largest at lower μ where fewer tracks are reconstructed. It is also apparent that all WPs exhibit non-linear behaviour. *TML* and *TMHPSL* display very similar behaviour that overshoot the linear fit at high μ, suggesting that the WPs accept a larger amount of fake tracks. *TMSPL* and *TMSPHPSL* also show very similar trends but instead undershoot the linear fits, suggesting that they are accepting fewer fake tracks and/or suffer from poor track selection efficiency.

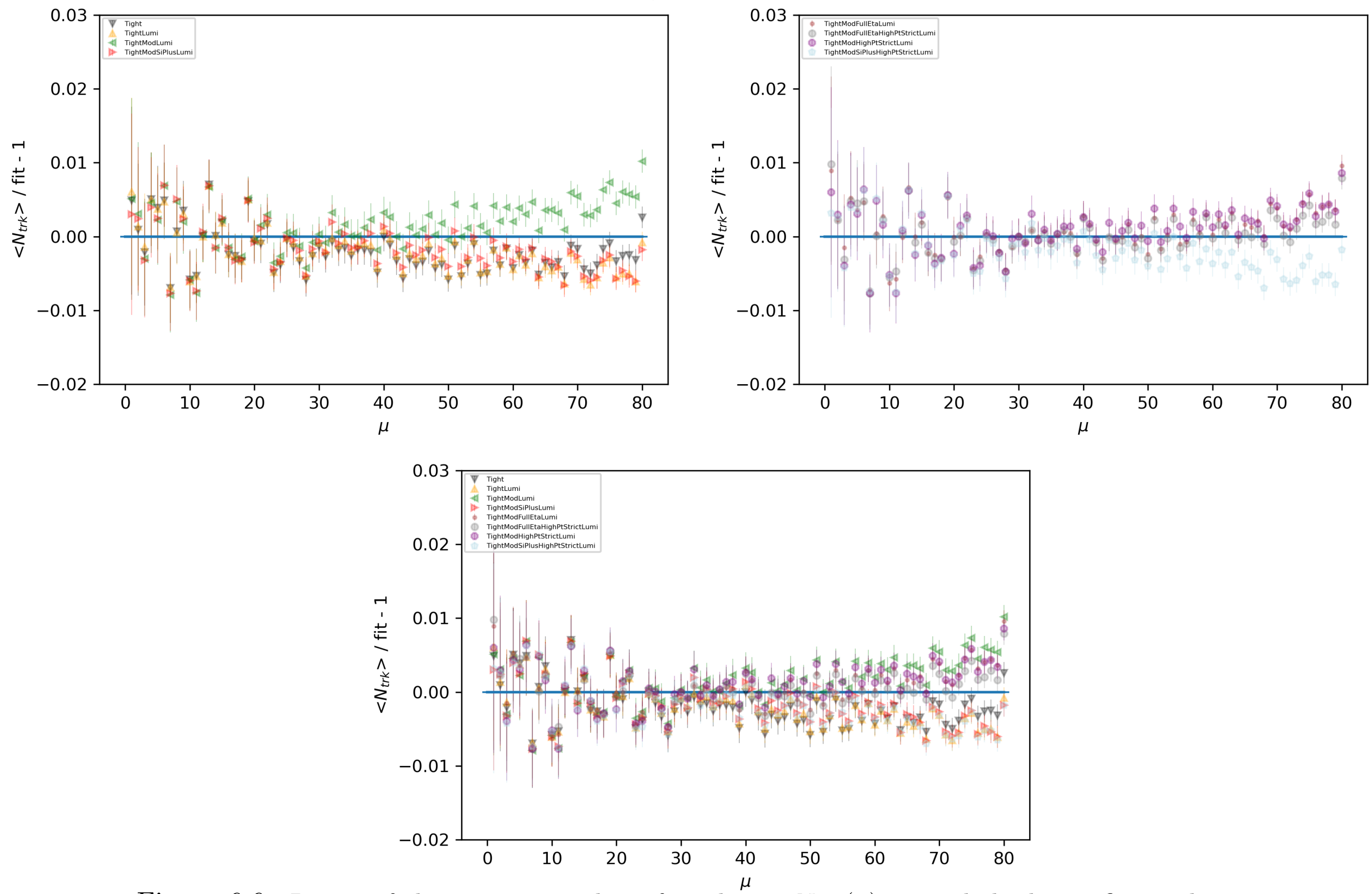

Figure 6.6: Ratios of the average number of tracks, $< N_{trk}(\mu) >$, and the linear fits made to $< N_{trk}(\mu) >$ between $\mu = 0$ and $\mu = 20$ for the different WPs. The Run 2 (top left) and Run 3 (top right) WPs are shown separately and together (bottom).

It is assumed that there are no significant non-linear effects in the range where the linear fits are made, between $\mu = 0$ and $\mu = 20$. The ratios provide information about the overall non-linear effects on the track averages but do not make it possible to see the individual contributions from the track reconstruction times selection efficiency or by the presence of fake tracks. To investigate the magnitude of these effects, and in order to compare the different WPs, further studies are proposed in Section 7.

7 Future work

The studies presented in this thesis could be continued by analysing the non-linear contributions in the track-counting luminosity measurement further. These are the track reconstruction times selection efficiency, $\epsilon_{r\times s}$, as well as the fake track rate, f_{fake}, both of which have a non-linear dependence on μ. These can both be determined in MC using the so-called truth record which keeps information on which particle in the simulation resulted in which reconstructed track.

7.1 Track reconstruction times selection efficiency

The track reconstruction times selection efficiency is defined as

$$\epsilon_{r\times s} = \frac{N_{trk}}{N_{true}}, \tag{7.1}$$

where N_{true} is the number of true charged particles and N_{trk} is the number of tracks selected given a WP.

7.2 Fake track rate

The fake track probability should also be considered and is given by

$$f_{fake} = \frac{N_{trk}^{fake}}{N_{trk}}, \tag{7.2}$$

where N_{trk}^{fake} is the number of fake tracks that pass a WP selection and N_{trk} are all the tracks that pass the WP. Where a fake track is a track that has no associated truth particle.

8 Conclusions

From the analysis of the MC generated samples, Section 5, it is apparent that the use of a physical hard-scatter interaction in the generation of the samples introduces tracks at low μ that are not expected to be present in experimental data. The use of a visible hard scatter in the MC generation of samples that are to be used in track counting studies should thus be avoided. The use of the unphysical SNPG as hard-scatter interaction proved to produce samples that closely match results expected in experimental data, due to the neutrino passing undetected through the ID.

The WPs *TMHPSL* and *TMFEHPSL* follow the linear fits best out of all the WPs. This reveals that the combined non-linear effect from the tracking efficiency and the fake tracks is smallest for these WPs. The WP *TMFEHPSL*, with a linear fit slope of 3.2, accepts more than twice the amount of tracks, on average, compared to *TMHPSL*, with a linear fit slope of 1.4. This trend is seen for all WPs with full η acceptance. The WPs *T*, *TL*, *TMFEL* and *TMFEHPSL* all have full η acceptance and are the WPs that accepted the most mean number of tracks.

The WPs with smaller η acceptances are the ones that accept the fewest tracks on average. But the smaller acceptance does not seem to affect the linearity of the track counting measurements. *TML* and *TMHPSL* both overshoot the linear fits at higher μ, indicating higher acceptance of fake tracks, while *TMSPL* and *TMSPHPSL* undershoot the linear fits in the same range.

These results preliminarily point to *TMHPSL* and *TMFEHPSL* being the nominal WPs to use in Run 3 pending further analysis of the fake track rate and track reconstruction and selection efficiency.

It is worth mentioning that the assumption that there are no non-linear effects present in the track-counting measurement in the μ range between $0 - 20$, could be incorrect. This could be determined by investigating the linearity of the μ-dependence of the fake track rate as well as of the track reconstruction times selection efficiency, see Section 7.

References

[1] Paul Moder. "Measuring luminosity with track counting in the ATLAS experiment". In: *PoS* ICHEP2020 (2021), p. 811. DOI: 10.22323/1.390.0811.

[2] Mary K. Gaillard, Paul D. Grannis, and Frank J. Sciulli. "The standard model of particle physics". In: *Reviews of Modern Physics* 71.2 (Mar. 1999), pp. 96–111. DOI: 10.1103/revmodphys.71.s96.

[3] David J. Griffiths and Darrell F. Schroeter. In: *Introduction to quantum mechanics*. Third. Cambridge, United Kingdom. Cambridge University Press, 2018. Chap. 5.1.1, pp. 201–202.

[4] *Standard Model of Elementary Particles*. [Accessed 15-09-2023]. 2023. URL: https://en.wikipedia.org/wiki/File:Standard_Model_of_Elementary_Particles.svg.

[5] Sutton C. *Higgs boson — physics*. Jan. 10, 2020. URL: https://www.britannica.com/science/Higgs-boson.

[6] *ENP - INFN-LNF*. [Accessed 14-09-2023]. Apr. 2020. URL: https://w3.lnf.infn.it/research/theoretical-physics/enp/?lang=en.

[7] Florian Bechtel. *The Underlying Event in Proton-Proton Collisions*. 2009. URL: https://cds.cern.ch/record/1446555.

[8] R. K. Ellis, W. J. Stirling, and B. R. Webber. *QCD and Collider Physics*. Cambridge Monographs on Particle Physics, Nuclear Physics and Cosmology. Cambridge University Press, 1996. DOI: 10.1017/CBO9780511628788.

[9] CERN. *Pulling together superconducting electromagnets*. [Accessed 16-08-2023]. URL: https://home.cern/science/engineering/pulling-together-superconducting-electromagnets.

[10] David G.C. Jones. *Large hadron collider*. Oct. 2023. URL: https://www.britannica.com/technology/Large-Hadron-Collider.

[11] CERN. *Accelerator report full house LHC*. [Accessed 21-08-2023]. URL: https://home.cern/news/news/accelerators/accelerator-report-full-house-lhc.

[12] CERN. *Large Hadron Collider*. [Accessed 02-09-2023]. URL: https://home.cern/science/accelerators/large-hadron-collider.

[13] *The CMS Experiment at CERN*. [Accessed 25-10-2023]. URL: https://cms.cern/detector.

[14] CERN. *LHC report colliding angle*. [Accessed 10-09-2023]. URL: https://home.cern/news/news/accelerators/lhc-report-colliding-angle.

[15] Peter W. Higgs. "Broken Symmetries and the Masses of Gauge Bosons". In: *Phys. Rev. Lett.* 13 (1964). Ed. by J. C. Taylor, pp. 508–509. DOI: 10.1103/PhysRevLett.13.508.

[16] Werner Herr and B Muratori. "Concept of luminosity". In: (2006). DOI: 10.5170/CERN-2006-002.361.

[17] *Public ATLAS Luminosity Results for Run-2 of the LHC*. URL: https://twiki.cern.ch/twiki/bin/view/AtlasPublic/LuminosityPublicResultsRun1.

[18] *Public ATLAS Luminosity Results for Run-1 of the LHC*. URL: https://twiki.cern.ch/twiki/bin/view/AtlasPublic/LuminosityPublicResultsRun2.

[19] The Associated Press. *World's biggest particle collider restarts after long break*. [Accessed 11-09-2023]. Apr. 2022. URL: https://www.ctvnews.ca/sci-tech/world-s-biggest-particle-collider-restarts-after-long-break-1.5872039.

[20] *Luminosity Public Results Run 3*. [Accessed 15-09-2023]. 2022. URL: https://twiki.cern.ch/twiki/bin/view/AtlasPublic/LuminosityPublicResultsRun3.

[21] *High Luminosity LHC - Technologies*. [Accessed 15-09-2023]. 2023. URL: https://home.cern/science/accelerators/high-luminosity-lhc/technologies.

[22] *Home - High Luminosity LHC Project*. [Accessed 15-09-2023]. URL: https://hilumilhc.web.cern.ch/.

[23] The ATLAS Collaboration. "The ATLAS Experiment at the CERN Large Hadron Collider". In: *Journal of Instrumentation* 3.08 (aug 2008). The ATLAS detector as installed in its experimental cavern at point 1 at CERN is described in this paper. A brief overview of the expected performance of the detector when the Large Hadron Collider begins operation is also presented., S08003. DOI: 10.1088/1748-0221/3/08/S08003.

[24] CERN. *The ATLAS experiment*. [Accessed 09-09-2023]. Apr. 14, 2021. URL: https://home.cern/science/experiments/atlas.

[25] Riccardo Maria Bianchi and ATLAS Collaboration. *Atlas Experiment Schematic Illustration*. Oct. 2022. URL: https://cds.cern.ch/record/2837191.

[26] *Glossary · GitBook*. [Accessed 23-08-2023]. URL: http://opendata.atlas.cern/books/current/get-started/_book/GLOSSARY.html.

[27] Izaak Neutelings. *CMS coordinate system*. [Accessed 02-09-2023]. Dec. 2022. URL: https://tikz.net/axis3d_cms/.

[28] *ATLAS inner detector: Technical Design Report, 1*. Geneva, 1997. URL: https://cds.cern.ch/record/331063.

[29] ATLAS Experiment. [Accessed 17-08-2023]. 2023. URL: https://atlas.cern/Discover/Detector/Inner-Detector.

[30] A Vogel. *ATLAS Transition Radiation Tracker (TRT): Straw Tube Gaseous Detectors at High Rates*. 2013. URL: https://cds.cern.ch/record/1514528.

[31] ATLAS Collaboration. "Experiment Briefing: Keeping the ATLAS Inner Detector in perfect alignment". General Photo. 2020. URL: https://cds.cern.ch/record/2723878.

[32] Federico Lasagni Manghi. *LUCID: The ATLAS Luminosity Detector*. Tech. rep. Geneva: CERN, 2019. DOI: 10.22323/1.340.0280.

[33] V Cindro et al. "The ATLAS Beam Conditions Monitor". In: *Journal of Instrumentation* 3.02 (Feb. 2008), P02004. DOI: 10.1088/1748-0221/3/02/P02004.

[34] Joao Pequenao. "Event Cross Section in a computer generated image of the ATLAS detector." 2008. URL: https://cds.cern.ch/record/1096081.

[35] *ATLAS Software Documentation*. [Accessed 02-09-2023]. July 2023. URL: https://atlassoftwaredocs.web.cern.ch/trackingTutorial/idoverview/.

[36] R. E. Kalman. "A New Approach to Linear Filtering and Prediction Problems". In: *Journal of Basic Engineering* 82.1 (Mar. 1960), pp. 35–45. ISSN: 0021-9223. DOI: 10.1115/1.3662552.

[37] CERN - ROOT. *TTree Class Reference*. [Accessed 02-06-2023]. 2023. URL: https://root.cern.ch/doc/master/classTTree.html.

[38] ATLAS Software Documentation. May 2023. URL: https://atlassoftwaredocs.web.cern.ch/AnalysisSWTutorial/basic_trees/.

[39] Stefano Frixione and Bryan R Webber. "Matching NLO QCD computations and parton shower simulations". In: *Journal of High Energy Physics* 2002.06 (June 2002), pp. 029–029. DOI: 10.1088/1126-6708/2002/06/029. URL: https://doi.org/10.1088%2F1126-6708%2F2002%2F06%2F029.

[40] J. Alwall et al. "The automated computation of tree-level and next-to-leading order differential cross sections, and their matching to parton shower simulations". In: *Journal of High Energy Physics* 2014.7 (July 2014). DOI: 10.1007/jhep07(2014)079. URL: https://doi.org/10.1007%2Fjhep07%282014%29079.

[41] Simone Alioli et al. "A general framework for implementing NLO calculations in shower Monte Carlo programs: the POWHEG BOX". In: *Journal of High Energy Physics* 2010.6 (June 2010). DOI: 10.1007/jhep06(2010)043. URL: https://doi.org/10.1007%2Fjhep06%282010%29043.

[42] Stefano Frixione, Paolo Nason, and Carlo Oleari. "Matching NLO QCD computations with parton shower simulations: the POWHEG method". In: *Journal of High Energy Physics* 2007.11 (Nov. 2007), pp. 070–070. DOI: 10.1088/1126-6708/2007/11/070. URL: https://doi.org/10.1088%2F1126-6708%2F2007%2F11%2F070.

[43] Paolo Nason. "A New Method for Combining NLO QCD with Shower Monte Carlo Algorithms". In: *Journal of High Energy Physics* 2004.11 (Nov. 2004), pp. 040–040. DOI: 10.1088/1126-6708/2004/11/040. URL: https://doi.org/10.1088%2F1126-6708%2F2004%2F11%2F040.

[44] B. Andersson et al. "Parton fragmentation and string dynamics". In: *Physics Reports* 97.2 (1983), pp. 31–145. ISSN: 0370-1573. DOI: https://DOI.org/10.1016/0370-1573(83)90080-7.

[45] S. Agostinelli et al. "Geant4—a simulation toolkit". In: *Nuclear Instruments and Methods in Physics Research Section A: Accelerators, Spectrometers, Detectors and Associated Equipment* 506.3 (2003), pp. 250–303. ISSN: 0168-9002. DOI: https://DOI.org/10.1016/S0168-9002(03)01368-8.

[46] Zachary Marshall and the ATLAS Collaboration. "Simulation of Pile-up in the ATLAS Experiment". In: *Journal of Physics: Conference Series* 513.2 (June 2014), p. 022024. DOI: 10.1088/1742-6596/513/2/022024.

[47] "ATLAS - 2018 pp data taking". In: *LuminosityPublicResultsRun2, AtlasPublic, TWiki* (2015). [Accessed 14-08-2023]. URL: https://twiki.cern.ch/twiki/bin/view/AtlasPublic/LuminosityPublicResultsRun2#2018_pp_data_taking.

[48] ATLAS Collaboration. *Luminosity determination in pp collisions at $\sqrt{s} = 13$ TeV using the ATLAS detector at the LHC*. 2022. arXiv: 2212.09379 [hep-ex].

[49] G et al. Avoni. "The new LUCID-2 detector for luminosity measurement and monitoring in ATLAS". In: *JINST* 13.07 (2018), P07017. DOI: 10.1088/1748-0221/13/07/P07017.

[50] G. Ripellino. *Haystacks and needles: Measuring the number of proton collisions in Atlas and probing them for the production of new exotic particles*. Licentiate Thesis. 2022. URL: https://urn.kb.se/resolve?urn=urn:nbn:se:kth:diva-312007.

[51] ATLAS InDet Tracking Performance Approved Plots. [Accessed 03-09-2023]. 2023. URL: https://twiki.cern.ch/twiki/bin/view/AtlasPublic/InDetTrackingPerformanceApprovedPlots

[52] ATLAS Software Documentation. [Accessed 15-08-2023]. 2023. URL: https://atlassoftwaredocs.web.cern.ch/athena/athena-releases/.